Nuclear Instruments and Methods in Physics Research A 666 (2012) 25–46

Contents lists available at SciVerse ScienceDirect

Nuclear Instruments and Methods in Physics Research A

journal homepage: www.elsevier.com/locate/nima

Review

# Silicon tracking detectors in high-energy physics

Frank Hartmann

*Institut für Experimentelle Kernphysik, KIT, Karlsruhe, Germany*

ARTICLE INFO

Available online 11 November 2011

*Keywords:*
Silicon sensors
Tracking detectors
Radiation hardness
SLHC
RD50
ILC
Vertexing

ABSTRACT

Since the fifties, semiconductors have been used as energy spectrometers, mainly in unsegmented ways. With the planar technique of processing silicon sensors in unprecedented precession, strip-like segmentation has allowed precise tracking and even vertexing, culminating in the early eighties with NA11 in the tagging of heavy flavor quarks—here the c-quark. With the later miniaturization of electronics, dense detector application was made possible, and large-scale systems were established in the heart of all LEP detectors, permitting vertexing in barrel-like detectors. At the time of LEP and the TEVATRON, tasks were still bifurcated. Small silicon detectors (up to three layers) did the vertexing and further out, gaseous detectors (e.g., drift chambers or time-projection chambers) with larger lever arms did the tracking. In RUN II of the CDF detector, larger silicon tracking devices, still complemented by a huge drift chamber, began to use a stand-alone tracking. At the LHC, ATLAS and CMS bifurcate in a slightly different way. Silicon pixel detectors are responsible for the vertexing, and large volume silicon strip detectors (up to 14 layers) are the main tracking devices. Silicon tracking systems are a fundamental part of modern multipurpose high-energy physics experiments. Despite the vertexing and thus the heavy quark tagging, silicon tracking detectors in combination with a strong B-field deliver the most accurate momentum measurement, and for a large range, also the best energy measurement.

In this paper, the functionality of pixel and strip sensors will be introduced, and historical examples will be given to highlight the different implementations of the past 30 years.



**Contents**



## 1. Principle

The concept will be introduced and the basic formulas will be listed without any real derivation. More basic and detailed discussions can be found in Refs. [1–6]. Simple designs of sensors and modules are presented along with their behavior under radiation, one of the current major issues of design and research due to their position close to the interaction point.

### 1.1. Basic sensor parameters

Silicon is a semiconductor, which is a solid matter that is isolated at low temperatures and shows a measurable

*E-mail address:* Frank.Hartmann@cern.ch

0168-9002/$ - see front matter © 2011 Elsevier B.V. All rights reserved.
doi:10.1016/j.nima.2011.11.005

conductance at higher temperatures. Its specific conductance of $10^2-10^{-9}\,\Omega^{-1}\,\mathrm{cm}^{-1}$ lies between that of metals and that of insulators. Silicon, the element that revolutionized the development of electronics, is known as an important material with many uses, dominating electronic technology today. Silicon sensors have an excellent intrinsic energy resolution: for every 3.6 eV released by a particle crossing the medium, one electron–hole pair is produced. Compared to the approximately 30 eV required to ionize a gas molecule in a gaseous detector, one gets 10 times the number of particles in silicon for the same energy. The average energy loss and high ionized particle number with $390\,\mathrm{eV}/\mu\mathrm{m}\sim 108$ (electron−hole pairs)/μm is effectively high due to the high density of silicon.

The usefulness and success of silicon can be explained in a handful of keywords:

- abundance;
- energy band gap;
- possibility of changing gap properties by defined adding of certain impurity atoms (dopants);
- the existence of a natural oxide;
- microscopic structuring by industrial lithography.

By adding Type III and Type V atoms, "p-type" and "n-type" material can be formed, which in combination form a "pn-junction". The surface of the sensor volumes of one type is then structured with the opposite type—the structures and the volume form a multitude of pn-junctions. Structuring can be strip- or pixel-like. The possibility of depleting the full sensor volume of free charge carriers by applying a "high" reverse bias voltage on the pn-junctions is one of the keys to success. The natural oxide allows passivation of the sensor but can also be easily used as an insulation oxide to allow in-sensor coupling capacitors. For the reverse-bias case, charge created in the space-charge region (SCR) can be collected at the junction (strips or pixels), while charge created in the non-depleted zone recombines with free majority carriers and is lost. Operation conditions, namely voltage $V_{external}$, is therefore such that the full volume is depleted. With $V_{external}=V_{bias}$ larger than the diffusion or built-in voltage from the pure pn-junction, the depletion zone width $w$ is

$$w=\sqrt{2\epsilon\varrho\mu V_{bias}} \tag{1}$$

and vice versa

$$V_{full\ depletion}=V_{FD}=\frac{D^2}{2\epsilon\mu\varrho} \tag{2}$$

where $w=D$ is the full sensor thickness, $\mu$ is the mobility and $\varrho$ is the bulk resistivity. $V_{FD}$ is one of the most important design parameters, describing the minimal operation voltage the sensor has to sustain without going into current breakdown. In material dominated by one type of impurity, e.g., if the donor dopant density $N_d$ is much larger than the intrinsic carrier concentration, the following expression for the resistivity $\varrho$ is valid:

$$\varrho=\frac{1}{e(\mu N_d)}. \tag{3}$$

The mobilities for electrons and holes are $\mu_e=1350\,\mathrm{cm}^2/\mathrm{V\,s}$ and $\mu_h=450\,\mathrm{cm}^2/\mathrm{V\,s}$, resulting in a readout time of approximately 10 ns in 100 μm thick silicon.

The second important operation parameter is the reverse current, also called leakage current or dark current, which defines power consumption; shot noise; and also potential warm-up, possibly resulting in thermal run-away. With $V_{bias}>V_{FD}$, the equilibrium is disturbed, and the established electrical field sweeps the thermally generated electron–hole pairs in the SCR out of the depletion region. The emission process is dominated by the Shockley–Read–Hall transitions, resulting in a reverse current described by

$$I_L=\frac{1}{2}e\frac{n_i}{\tau_L}w\cdot A \tag{4}$$

with the surface $A$ of the junction, $w$ thickness (basically volume), the intrinsic carrier density $n_i$ and the generation lifetime $\tau_L$ as a main parameter. In short, the leakage current is completely dominated by the effective lifetime $\tau_L$ (the generation lifetime of minority carriers). The impurity states $N_t$ near mid-gap, e.g., Au and all novel metals, are "*lifetime killers*". The temperature dependency enters indirectly via $n_i\times T^2\propto e^{E_g/2kT}$ with band gap $E_G$ and Boltzmann constant $k$.

The current increases linearly with $w\propto\sqrt{V}$ until the detector is fully depleted. At higher bias voltage an electrical breakdown is observed, where the current starts to increase dramatically. The breakdown can be explained either by "*avalanche breakdown*", due to charge multiplication in charge collisions with the lattice, or by "*Zener breakdown*, based on the quantum mechanical *tunnel effect*. Fig. 1 shows $I\propto\sqrt{V}$ behavior as well as a breakdown.

To determine the depletion voltage, the capacitance to voltage dependency is exploited. The full capacitance of a sensor can be calculated by regarding the two planes of the SCR as a plate capacitor with silicon as the dielectric inside. The bulk capacitance $C$ decreases linearly with $w$, and therefore $\sim\sqrt{V}$:

$$C_{bulk}=\begin{cases}A\sqrt{\dfrac{\epsilon_{Si}}{2\varrho\mu V_{bias}}}, & V_{bias}\le V_{FD}\\ A\dfrac{\epsilon_{Si}}{D_{depletion}}=const., & V_{bias}>V_{FD}.\end{cases} \tag{5}$$

Fig. 1 expresses the dependence of $C$ and $V_{FD}$ on area, thickness and $\varrho$. The capacity–voltage characteristic CV or $1/C^2$ vs. voltages behavior is used as a standard method to determine $V_{FD}$. The kink determines $V_{FD}$.

The last important basic parameter to be mentioned here is the electrical field resulting from the applied bias voltage. The field has its maximal strength at the main junction, e.g., the segmented face in a p-in-n sensor before irradiation with $E_{MAX/MIN}=(V\pm V_{FD})/D$ at the faces. The sensor design (geometry and $V_{FD}$) has to guarantee that the field is always below the break down voltage of silicon or, with some tricks described later, below the breakdown voltage of $SiO_2$.

In addition to these more bulk-like properties, surface interfaces must also be monitored carefully to guarantee low parasitic and load capacities, and surface currents must be kept low to guarantee segmentation isolation.

### 1.2. Silicon strip and pixel sensors; operation principle

All tracking detectors make use of the free charges resulting from the ionization of a passing charged particle in a medium, e.g., a gas or a semiconductor. The average charge loss of a charged particle in a medium is described by the Bethe-Bloch formula:

$$-\frac{dE}{dx}=4\pi N_A r_e^2 m_e c^2 z^2\frac{Z}{A}\frac{1}{\beta^2}\left[\frac{1}{2}\ln\left(\frac{2m_e c^2\beta^2\gamma^2 T_{max}}{I^2}\right)-\beta^2-\frac{\delta(\gamma)}{2}\right]. \tag{6}$$

In this formula, $z$ is the charge of the incident particle, $T_{max}$ is the maximum kinetic energy that can be imparted to a free electron in a single collision, $I$ is the mean excitation energy, $Z$ is the atomic number, $A$ is the atomic mass, $N_A$ is Avogadro's number, $m_e$ is the mass of an electron, $c$ is the speed of light, $r_e$ is the classical electron radius, $\beta=v/c$ and $\gamma=1/\sqrt{1-\beta^2}$ and $\delta$ is the density effect correction. A more detailed description can be found in Ref. [7]. The most prominent part is the minimum at approximately $\beta\gamma=3$,

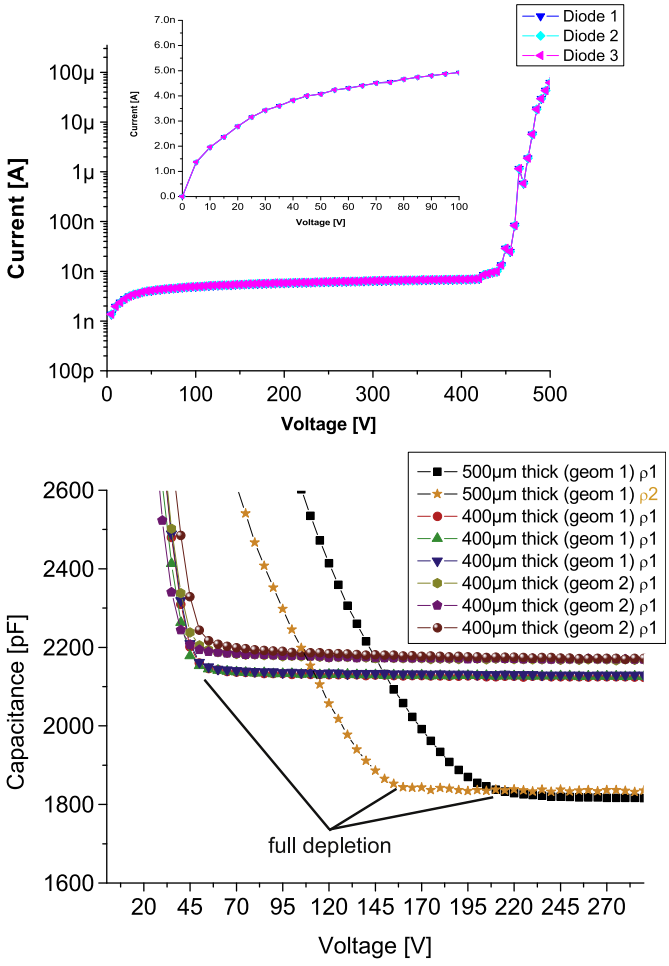


**Fig. 1.** The current voltage characteristic for a Si-diode in the reverse-bias direction is depicted. The expanded view shows the $I \propto \sqrt{V}$ dependence, while the global view shows the full scan, including breakdown at a higher voltage. On the lower figure the measurement plots describe the capacitance's dependence on area and thickness quite clearly. The *x*-axis coordinate of the kink determines the depletion voltage, defined by material resistance and thickness. The *y*-coordinate of the plateau shows the minimal capacitance, defined by area and thickness. The two upper bands depict sensors of two different geometries with slightly different areas and the same high resistivity material, both $D = 400$ µm thick. The lower CV curves describe $D = 500$ µm thick sensors. With increased thickness, $C$ becomes smaller and $V_{depletion} \propto D^2$ becomes larger. The different depletion voltages of the lower curves derive from two different resistivities $\varrho 2 > \varrho 1$.

expressing the minimum of deposited energy in the medium. Every detector must be designed to be able to detect these *M*inimum *I*onizing *P*articles (MIPs) with the minimum deposited energy, i.e., the noise level must be lower than the resulting number of electron holes. In addition, there are statistical fluctuations. Both the number of collisions in a finite medium and the energy transfer per scattering vary. The first effect can be described by a Poisson distribution, while the second is described by a "straggling function" first deduced by Landau. In rarer cases, called δ-rays or δ-electrons, the transferred energy is large. These δ-electrons are responsible for the asymmetric long tail towards high charge deposits. Overall, the most probable value of energy transfer is about 30% lower than the average value. For silicon, the average energy used for the creation of one electron–hole pair in the indirect semiconductor is 3.6 eV, about three times larger than the band gap of 1.12 eV, because part of the deposited energy is used for phonon creation. For a MIP, the most probable number of electron–hole pairs generated in 1 µm of silicon is 76, while the average is 108.

The working principle of a silicon microstrip detector is illustrated in Fig. 2.

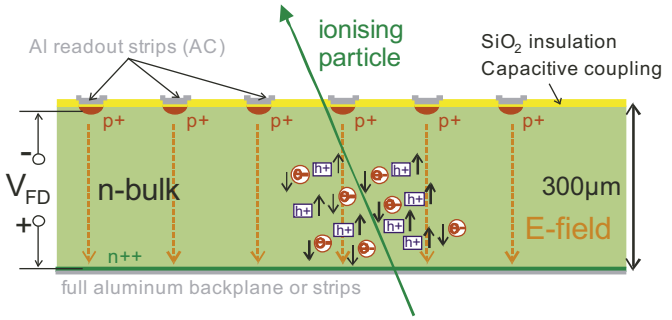


**Fig. 2.** Working Principle of an AC-coupled Silicon Micro-Strip Detector. Electron–hole pairs resulting from the ionization of the crossing charged particle, according the Bethe-Bloch-formula, travel to the electrodes on the sensor planes. The segmentation into individual pn-junctions makes it possible to collect the charges on a small number of strips only, where they capacitively couple to the Al readout strips. The latter are connected to the readout electronics, where the intrinsic signal is shaped and amplified. In the case of segmented p strip implants in an n-bulk silicon material, holes are collected at the p strips.

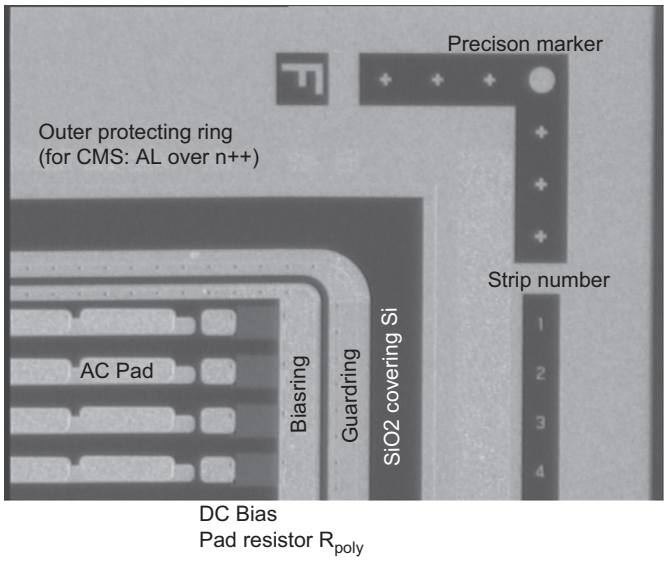


**Fig. 3.** The top-view of a sensor, the ring structures, n++ active edge protecting ring, the guard ring and the bias ring are visible. Both the guard and bias ring are Al structures located on top of the p+ implants, where they are directly contacted. Precision markers are needed to enable a precision assembly, while the strip numbers facilitate problem reports during quality assurance. The bias resistors connect the p+ strip located below the aluminum strips to the bias ring. A number of AC-pads are processed at the end of the strips to enable several connections to the readout electronics. The DC-pad, a direct contact to the p+ strip enables probing.

An ionizing particle penetrates through a fully depleted silicon n doped slice. The generated holes drift along the electrical field created by the bias voltage to the p doped strips.[1] while the electrons drift to the n+ backplane. The charges collected on the doped strips are then induced, by capacitive coupling, to the aluminum readout strips, which are directly connected[2] to the charge-preamplifier of the readout chip. In principle, the capacitor does not need to be implemented on the wafer; it can also be instrumented inside the readout chip or in between, as in the case of the NA11 [18] experiment. Sensors with integrated capacitors are called AC-coupled; others are DC-coupled. Because the capacitor needs to be large, the full strip length consists of a p+ oxide metal sandwich, as

[1] In an n-in-n, n-in-p or a double sided detector, electrons drift to the n+ doped strips.

[2] Most often by ultrasonic wire-bonding.

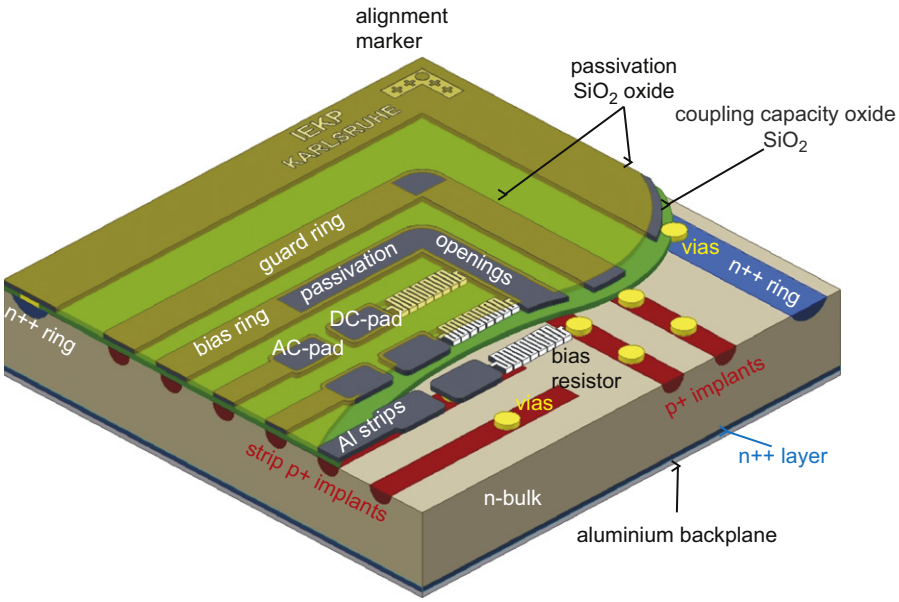


**Fig. 4.** A sketch of a 3D schematic showing the baseline of the CMS sensor at the LHC and could represent essentially any single sided AC-coupled $R_{poly}$ biased sensor. In operation, the bias ring is connected to the GND potential, which is then distributed to the p+ implant strips, while the Al backplane is set to positive high voltage depleting the full n-bulk volume by forming a pn-junction p+ strip to n-bulk. The coupling capacitor is defined between the aluminum strip and p+ implant; the inter-strip capacity is defined between neighboring strips (both p+ and Al part). The guard ring shapes the field at the borders. The n++ ring defines the volume and prevents high field in the real, not smooth, cut edge regions [5].

in the DELPHI (Section 2.2), CDF (Section 2.3) and CMS experiments (Section 2.4). The Si to $SiO_2$ affinity allows easy integration of a capacitive coupling of diode to metal contact, thereby allowing the use of a charge-amplifying chip. A top-view photo of a sensor with descriptions of the diverse sensor elements is presented in Fig. 3. A full functional description of the necessary periphery – shown in Fig. 3 – such as the bias ring, guard ring and active edges is beyond the scope of this document. A more exhaustive description can be found in Ref. [5]. Fig. 4 displays a three-dimensional view of a standard single-sided sensor design—the main elements are described in the caption. It should be mentioned that segmentation of the bulk silicon material can be done on both sides with many benefits but also with many additional problems. The obvious benefit is a two-dimensional readout with different strip orientation on each side[3] of a single sensor. Strip implants are then composed of p+ and n+ on the two sides, called the junction and ohmic sides, respectively. The ohmic side, with n+ strips in an n-bulk needs special attention to arrange strip isolation due to the presence of an electron accumulation layer with additional p+ doping in between n+ strips or electron repelling field plates (the same isolation criteria applies for n-strips in a p-bulk). Fig. 5 presents the ultimate technology mix: a double-sided sensor with integrated coupling capacitors, serving also as a field plate on the n-side; bias voltage supplied via polysilicon resistors; and finally a double metal layer to allow perpendicular strip routing. Fig. 6 shows the top view of DELPHI double-sided sensors.

The final position of the penetration is then calculated by analyzing the signal pulse height distribution on all affected strips. The strip pitch is a very important parameter in the design of the microstrip sensor. In gaseous detectors with a high charge multiplication, a signal distribution over several sense wires is helpful to reconstruct the shape of the charge distribution and find the charge deposited center. In silicon detectors, there is no charge multiplication, and small charges would be lost in the noise distribution. Therefore, signal spreading over many strips could result in a loss of resolution. For single-strip, events the track position is given by the strip number. For tracks generating enough charge on two strips to exceed the threshold value, the position can be determined more precisely either by calculating the "center of gravity"[4] or with an algorithm that takes into account the actual shape of the charge distribution[5] and the acceptance of the sensor. In short, the resolution with analog readout is given by

$$\sigma_x \propto \frac{pitch}{signal/noise}. \tag{7}$$

As a result, sensors with a pitch of $p=25$ μm and a signal/noise ($S/N$) of 50 have a position resolution of 2−4 μm. Additional intermediate implant strips between readout strips improve the resolution further by capacitively coupling to the readout strips. This technique helps to minimize the number of electronic channels while achieving an adequate position resolution. For digital readout, the position resolution is given by $\sigma_x \approx p/\sqrt{12}$.[6]

Another method to achieve a two-dimensional readout would be a pixelated segmentation. From the sensor point of view the design and processes are marginally different in the first approximation. The main difference is the connectivity to the electronics. With the pixelated small sensor cell about the equivalent size of the corresponding readout cell, the readout covers the full sensor area, and channels are "bump-" or "flip-chip"-bonded, while strip-like sensor cells reach the end of the sensor and the much smaller electronics chip can be wire-bonded. A scheme can be seen in Fig. 7. The sandwich is often called a Hybrid Active Pixel Sensor (HAPS). These descriptions represent the main pixel species in the field of High Energy Physics, while in other areas, Charged Coupled Devices (CCDs) or Monolithic Active Pixels (MAPS) (CMOS) sensors are in more common use. However, they are either too slow or not sufficiently radiation hard for the current collider environment.

[3] Common strip orientations are 90° or a small stereo angle like 0.1–2°.

[4] Assuming a uniform charge distribution, a track crossing between two strips at $\frac{3}{4}\times$ *pitch* will store $\frac{1}{4}\times$ *charge* on the left strip and $\frac{3}{4}\times$ *charge* on the right strip.

[5] Approximately a Gaussian distribution, due to the diffusion profile.

[6] $\sigma_x \approx p/\sqrt{12}$ arising from geometrical reflections: $\langle \Delta x^2 \rangle = (1/p)\int_{-p/2}^{p/2} x^2\, dx = p^2/12$.

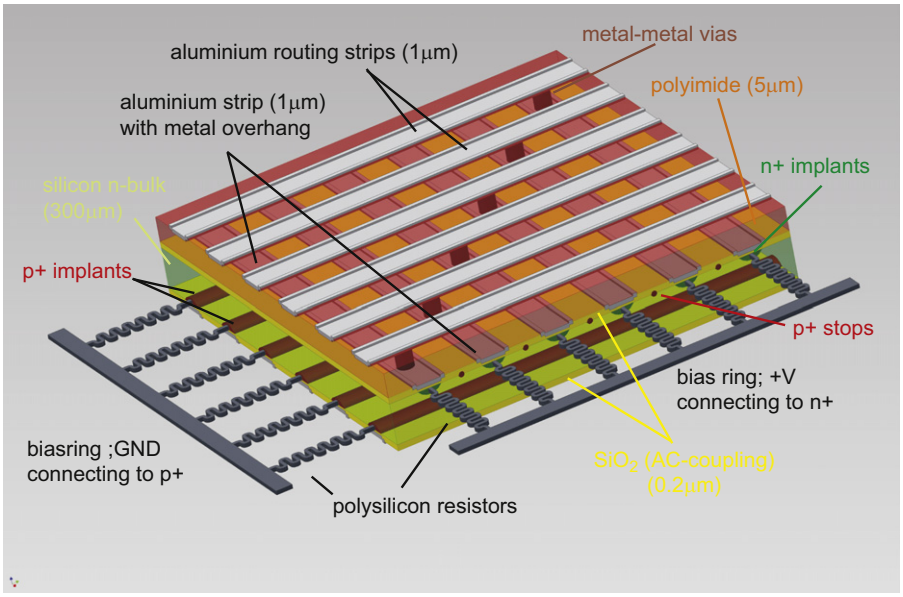


**Fig. 5.** The DELPHI double sided, double metal sensor scheme. The sensors contain novel integrated coupling capacitors. The bias is applied via highly resistive polysilicon resistors. The n-side strips are routed via a second metal routing layer, and the innovative field plate configuration guarantees 100 MΩ n strip isolation [5].

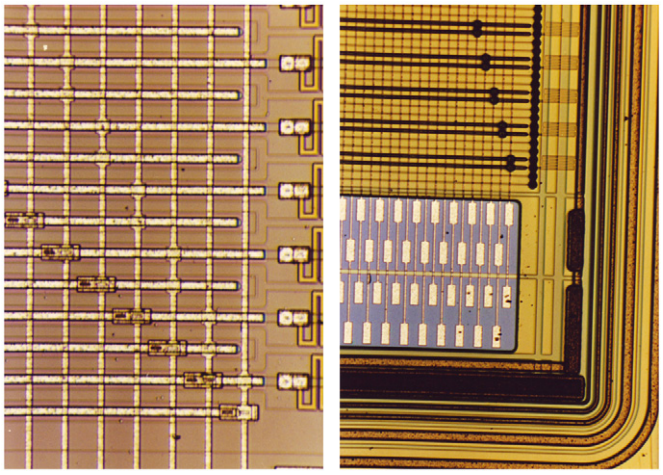

**Fig. 6.** The left-hand photo shows the microscopic view of the n-side of a double sided sensor from the DELPHI experiment. The right-hand picture shows a single-sided sensor. The perpendicular strip arrangement with the contact "vias" can be seen on both pictures. Both sensors are using the double metal routing to connect the strips to the readout channels. The meander structures, the polysilicon resistors, connect the bias voltage to the implants. The polysilicon length and narrow shape defines the high resistance. In the left-hand picture of the n-side structure, the p+ stop structures surrounding every second implant are clearly visible. They are responsible for the strip-to-strip isolation. The sensor on the right is also interesting; two metal strips are always connected together with two non-metalized intermediate strips (implants only) in between. With a 50 μm implant pitch, this arrangement gives a 200 μm readout pitch with good charge sharing. The intermediate strips were connected to the bias ring via bias resistors on the other end of the sensor to guarantee a uniform potential on all implants. For the sensor on the left every single strip is connected to the readout. This illustration should give a general idea of the variety of sensors in the DELPHI detector.

### 1.3. Irradiation damage

Tracking detectors are situated in the heart of the large HEP detectors, as close as possible to the particle interactions, and therefore suffer a harsh environment. Traversing particles not only ionize the lattice but also interact with the atomic bodies via the electromagnetic and strong forces. Atoms can be displaced to create interstitials ($I$), vacancies ($V$) and more complex constructs, e.g., di-vacancies ($V_2$) or even triple-vacancies ($V_3$). Di-interstitials ($I_2$) are also common. All these defects deform the lattice. In addition, diffusing Si atoms or vacancies often form combinations with impurity atoms, such as oxygen, phosphorus or carbon, again with different properties. Radiation fluence grows with increasing integrated luminosity and lower radius. It should be mentioned here that different particles do different amounts of damage: lower-energy charged particles incite more point-like defects, while higher energy charged particles and neutral particles (e.g., neutrons) do more cluster-like damage. For materials (n-bulk floatzone) used in current detectors, the damage by different particles can be normalized to "1 MeV neutron equivalent" damage by the Non-Ionizing Energy Loss NIEL hypothesis, and most fluence numbers are given using this normalization. Thanks to dedicated research and development collaborations, e.g., RD48 and RD50 [8], and enormous effort from HEP-detector collaborations, the current understanding of radiation damage and its time evolution is quite sufficient to design current TEVATRON and LHC experiments and operate them for many years. The basics of radiation damage are presented in Refs. [9–11], and recent studies on fully segmented sensors on a large sample can be found in Refs. [12,13]; a summary can be found in Ref. [5]. The three main effects (bulk and surface defects) introduced by radiation are

- displacement of atoms from their positions in the lattice (bulk);
- transient and long-term ionization in insulator layers (surface);
- formation of interface defects (surface).

This section will explain mainly the bulk defects, namely

- at $10^{14}$ $n_{1\ MeV}/cm^2$, the main problem is the increase of leakage current;
- at $10^{15}$ $n_{1\ MeV}/cm^2$, the high resulting depletion voltage is problematic, increase of $N_{eff}$;
- at $10^{16}$ $n_{1\ MeV}/cm^2$, the fundamental problem is the CCE degradation.

Fig. 8 shows the correspondence of deep energy levels in the band gap and their macroscopic electrical counterparts. The WODEAN

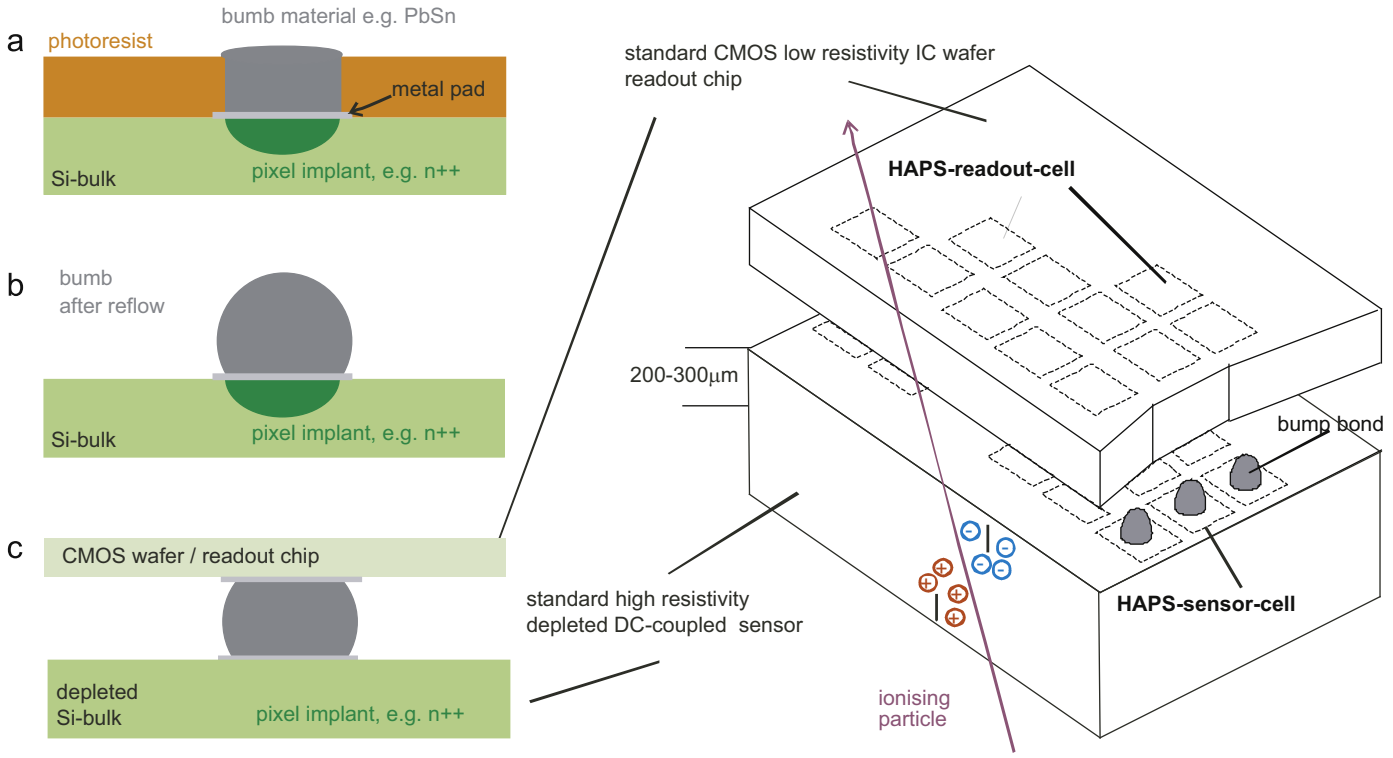


**Fig. 7.** Scheme of a *Hybrid Active Pixel Sensor* (HAPS). A HAPS is a sandwich of a silicon sensor and a standard CMOS readout chip. The sensor is of the high resistivity depleted DC-coupled type. The readout chip is realized in standard CMOS technology on a low resistivity wafer, the same size as the sensor and its readout cells are distributed in the same "pixelated" way as the sensor pixels. The merging is realized via "bump bonding" or "flip-chip-bonding". After preparing the pads with a dedicated under-bump-metallization a further lithography step opens holes on each pad in which to place the bump metal (a), e.g., Cu or In. After removing/etching the photoresist the metal undergoes another temperature step, the reflow to form balls of metal (b). The chip is then "flipped", aligned and pressed onto the sensor and warmed up for reflow, connecting sensor channels to readout cells (c).

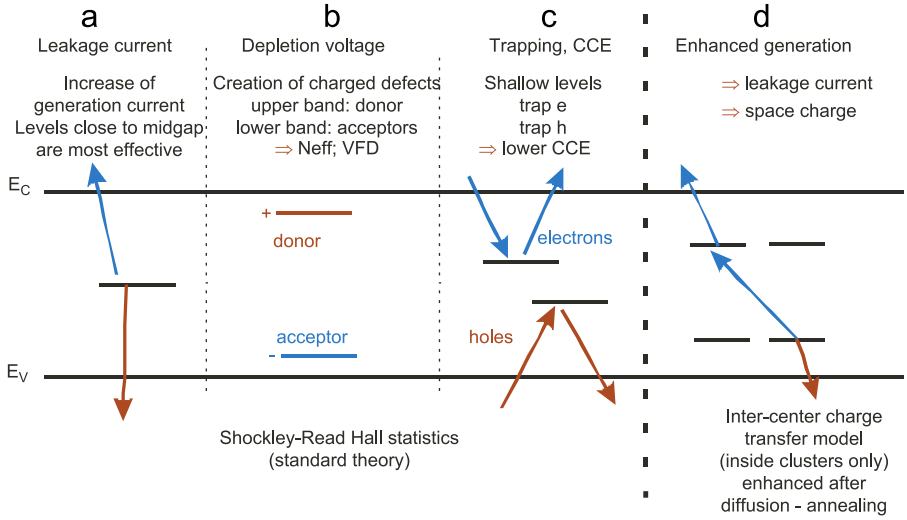


**Fig. 8.** The different defect level locations and their effects. All relevant defect levels due to radiation are located in the forbidden energy gap. (a) Mid-gap levels are mainly responsible for dark current generation, according to the Shockley–Read–Hall statistics, and for decreasing the charge carrier lifetime of the material. (b) Donors in the upper half of the band gap and acceptors in the lower half can contribute to the effective space charge. (c) Deep levels, with trapping times larger than the detector electronics peaking time, are detrimental. Charge is "lost"; the signal decreases and the charge collection efficiency is degraded. Defects can trap electrons or holes. (d) The theory of the inter-center charge transfer model says that combinations of the different defects in defect clusters can additionally enhance the effects.

and RD50 collaborations are systematically improving the qualitative understanding of microscopic defects and macroscopic degradation with respect to radiation of different particles and annealing evolution. It should be mentioned that the levels shown in Fig. 8 can be introduced by irradiation bulk defects or by initial impurities.

To understand the voltage, current or charge trapping (Charge Collection Efficiency, CCE) of an irradiated sensor the following mechanisms must both be taken into account

1. the damage to the lattice created by traversing particles;
2. the following diffusion processes—annealing.

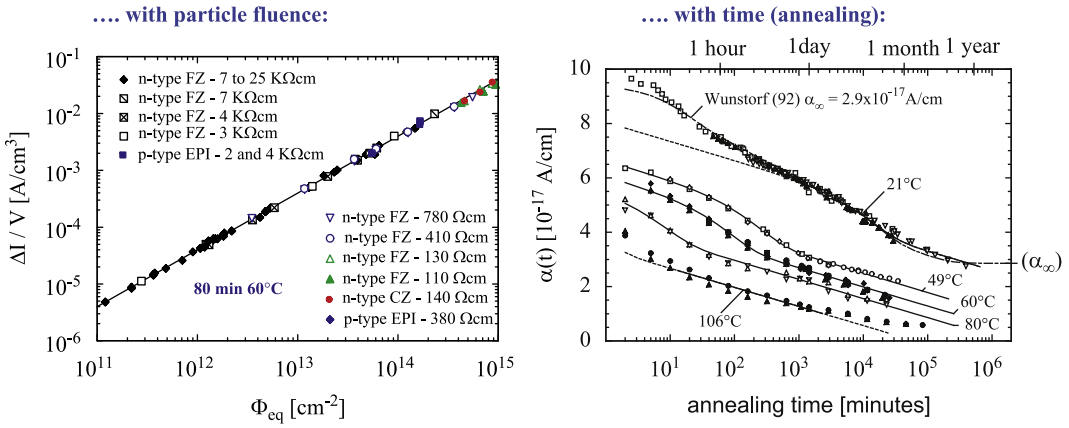


**Fig. 9.** Leakage current vs. fluence and annealing time [10,9].

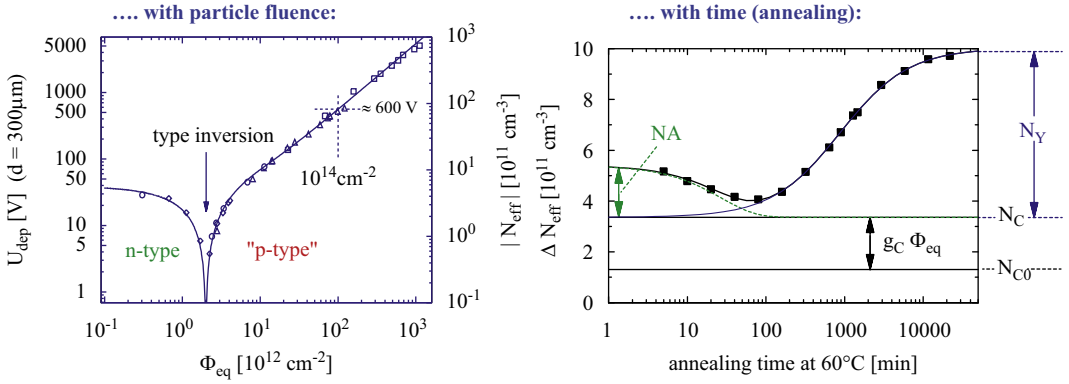


**Fig. 10.** Depletion voltage current vs. fluence and annealing time [9].

*Leakage current*: The current evolution with respect to fluence and time is shown in Fig. 9. It has been found in many experiments[7] that there is a linear relationship between dark current and fluence:

$$\frac{\Delta I}{V} = \alpha \Phi_{eq} \tag{8}$$

where $V$ normalizes for a given volume. $\alpha$ is called the current-related damage rate. The strong linearity over several orders of magnitude allows the technical use of diodes to determine the particle fluence by the increase in current. Mid-gap levels are mostly responsible for the current increase. During annealing, current always decreases.

*Depletion voltage*: The situation for the effective space-charge concentration is a bit more difficult. The evolution of the depletion voltage $\sim N_{eff}$ with fluence and with time is displayed in Fig. 10. Starting with an n-type doped silicon bulk, a constant removal of donors ($P+V \rightarrow VP$-center) together with an increase of acceptor-like levels (one example is $V+V+O \rightarrow V_2O$) shifts the space charge first down to an intrinsic level and then up to a more p-like substance. The material "type inverts". The depletion voltage therefore drops first and starts rising later. With

$$N_{eff} = N_{D,0} e^{-c_D \Phi_{eq}} - N_{A,0} e^{-c_A \Phi_{eq}} - b\Phi_{eq} \tag{9}$$

the evolution of $N_{eff}$ can be parameterized to a first approximation with the donor and acceptor removal rates, $c_D$ and $c_A$, plus the most important acceptor creation term, $b\Phi_{eq}$. The temperature-dependent diffusion[8] of $N_{eff}$ with time can be described by

$$\Delta N_{eff}(\Phi_{eq},t,T) = N_{C,0}(\Phi_{eq}) + N_A(\Phi_{eq},t,T) + N_Y(\Phi_{eq},t,T) \tag{10}$$

where $\Phi_{eq}$ stands for 1 MeV neutron equivalent fluence, with the stable term $N_{C,0}$, the short-term annealing term $N_A$ and the second-order long-term $N_Y$. This description is called the Hamburg Model, and it is depicted in the right part of Fig. 10. The details of formula (10) are beyond the scope of this paper; the decays can be described in first-order by a sum of exponential decays with different time constants for the beneficial ($N_A$) and the reverse term ($N_Y$). It must be mentioned that the exponential time constants of the beneficial term and the reverse term are substantially different, e.g., $\tau_a$ at 20 °C = 55 h and $\tau_y$ at 20 °C = 475 d. It should thus be stressed that even with the initial parameters given in Ref. [9], a re-fit is needed for each particular use case, e.g., new sensors or a different vendor.

The evolution of $N_{eff}$ begins to be a real problem as soon as the effective depletion voltage is above the applicable bias voltage, due to break down, thermal run-away or technical service restrictions. With the actual annealing time constants, any evolution can be frozen by keeping the sensors always below zero degrees, which is also true for charge trapping.

The description above is not exhaustive. It is mainly valid for n-bulk floatzone material. The behavior can be positively tuned by the introduction of oxygen or negatively by carbon—see Fig. 11.

[7] This is true for all materials so far, n-bulk, p-bulk, FZ, Cz, MCz, EPI, oxygenated.

[8] The term "diffusion" used here is a descriptive one combining effects such as diffusion, migration, break-up and re-configuration of defects—also often summarized by the term "annealing".

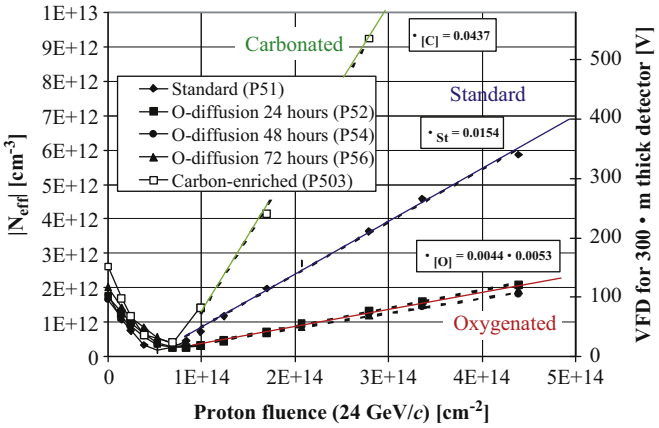


**Fig. 11.** Evolution of $V_{FD}$ vs. time of differently engineered silicon diodes. The beneficial influence of oxygen and damaging effect of carbon are clearly visible. Today, the ATLAS and CMS pixel sensors are composed of oxygenated silicon sensors. [Courtesy of RD48 and RD50.]

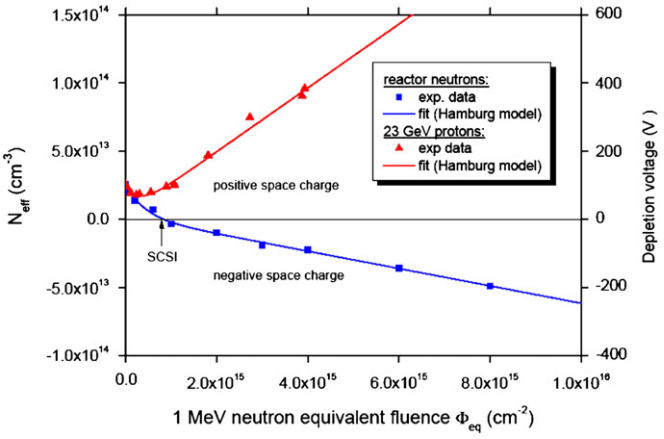


**Fig. 12.** Change of $N_{eff}$ in EPI-DO material vs. irradiation with different particles. Acceptor introduction is enhanced for neutron irradiation, similar to n-FZ material, while protons generate mainly donors. In the corresponding study the deep level states have been identified using the Thermal Stimulated Current (TSC) method [14].

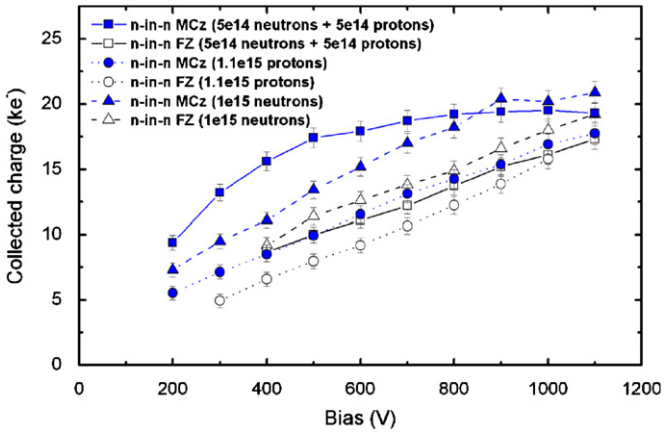


**Fig. 13.** Charge collection efficiency of MCz and FZ detectors after a total dose of $1 \times 10^{15}$ $n_{eq}cm^{-2}$ obtained with neutrons only, 26 MeV protons only or mixed (equal dose of neutrons and 26 MeV protons) irradiation. The CCE of the mixed irradiation is roughly the average of the protons and neutrons for the FZ sensors, while mixed irradiation improves the CCE at low bias voltages for the MCz sensors relative to neutron- or proton-only irradiations, indicating a compensation effect (with decrease of the $|N_{eff}|$) between the neutron- and proton-induced damage [15].

For other materials, e.g., Czochralski[9] (Cz), magnetic Czochralski (MCz) or exitaxial EPI grown silicon the situation becomes more complicated. Different radiation particles introduce different defects acting as acceptors or as donors (see Fig. 12).

Damage from neutrons produces irradiation damage compensating for that induced by protons (see Fig. 13). The compensating effect can even prevent type inversion (see Fig. 14).

For future devices, the chosen detector technology must be evaluated for different particle irradiation and for mixed fluences mimicking the final operational situation.

*Charge trapping*: The trapping rate is proportional to the concentration of trapping centers $N_i$ resulting from defects. In first order, the fluence dependence is linear and can be written as

$$N_i = g_i \Phi_{eq} f_i(t) \Rightarrow \frac{1}{\tau_{eff}} = \gamma \Phi_{eq} \tag{11}$$

where the introduction rate $g_i$; $f_i(t)$ describes the annealing with time. The slope $\gamma$ is different for electron and hole trapping, which are differently affected due to their different mobilities. The $f_i(t)$ is again, in first order, a sum of exponentials, but its effects are small. The degradation of *C*harge *C*ollection *E*fficiency (CCE) can

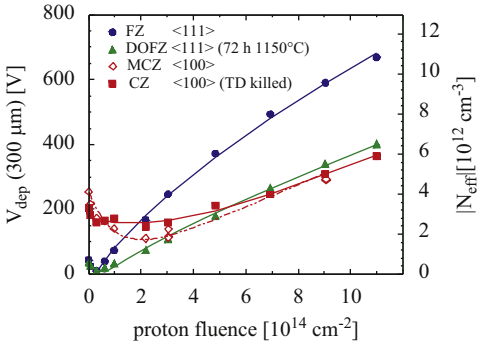


**Fig. 14.** Czochralski and magnetic Czochralski do not exhibit the distinct point of space-charge sign inversion, as seen for the standard or the diffused oxygenated floatzone material [39]. Deeper investigation using the Transient Current Technique (TCT) shows a more complicated $N_{eff}$ distribution in the silicon bulk, leading to a distinct double junction on the front and back sensor face.

then be described by

$$Q_{e,h}(t) = Q_{0_{e,h}} \exp\left(-\frac{1}{\tau_{eff_{e,h}}} \cdot t\right) \quad \text{where} \quad \frac{1}{\tau_{eff_{e,h}}} \propto N_{defects}. \tag{12}$$

[9] The Cz ingot, pulled from a melt, is naturally oxygen enriched due to the melt environment. The applied magnetic field for MCz damps oscillations and homogenizes the oxygen distribution.

At effective fluences of $10^{15}\Phi_{eq}$ and above, trapping becomes the most limiting factor of silicon usage as a particle detector. The charges no longer arrive at the collecting electrodes in 300 μm thick sensors. Examples of charge travel distances $x$ for $\Phi_{eq}=10^{15}$ $n_{1\ MeV}/cm^2$ and $\Phi_{eq}=10^{16}$ $n_{1\ MeV}/cm^2$ are:

- $\tau_{eff}(10^{15}\ n_{1\ MeV}/cm^2)=2$ ns:
  $x=v_{sat}\cdot\tau_{eff}=(10^7\ cm/s)\cdot 2\ ns=200\ \mu m$;
- $\tau_{eff}(10^{16}\ n_{1\ MeV}/cm^2)=0.2$ ns: $x=(10^7\ cm/s)\cdot 0.2\ ns=20\ \mu m$.

Trapping is basically material independent but strongly dependent on the charge collected (holes or electrons). It has to be mentioned that the discussed trapping description is mainly valid for the current n-bulk floatzone material, and some additional effects are described in Section 3.

### 1.4. Silicon strip and pixel modules

In the course of development of detectors, the area of silicon sensors increased while the electronic circuits underwent several miniaturization processes. Dedicated modules were developed to equip several detector barrel layers and forward structures with the least amount of material but the best uniform coverage. A module is the smallest unit containing, normally, one support structure; one to eight daisy-chained sensors plus one to several electrical circuits, called hybrids, containing some passive components; the front-end ASIC; and possibly some control units, multiplexers, and other components. Often, customized modules have been chosen to reach this goal, but with larger detectors such as the outer layers of the CDF detector, ATLAS or CMS simpler module designs were driven more by the constraints of mass production and final assembly. The size of the DELPHI detector still allowed individual solutions for the different layers and even different positions along the beam pipe. An inner silicon module of four sensors and its hybrid can be seen in Fig. 15, while the outermost layer modules of the last upgrade consisted of eight sensors. All were constructed manually on dedicated jigs and precise coordinate-measurement machines. Hybrids are placed at the end of the modules, outside the sensitive detector volume in essentially all LEP detectors and also most TEVATRON detectors.

With 15 232 modules in total, the CMS approach had to be much more conservative. The basic design can be seen in Fig. 16.

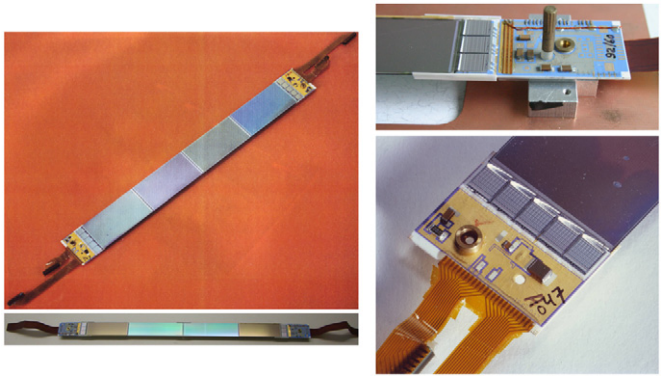

**Fig. 15.** A Delphi Inner and Outer Module. Each hybrid reads out two detectors with the daisy-chained strips connected to each other and to the amplifiers by wire-bonding. This assembly is chosen to carefully situate the electronics outside the active volume, thereby minimizing the material budget and also minimizing multiple scattering. The outer detector module contains five chips with a total of 640 strips on each hybrid side, while the inner detector module, being narrower, contains only three chips with 384 strips per side. The right part shows two generations of hybrids with their MX and Triplex chips bonded to a row of silicon sensors.

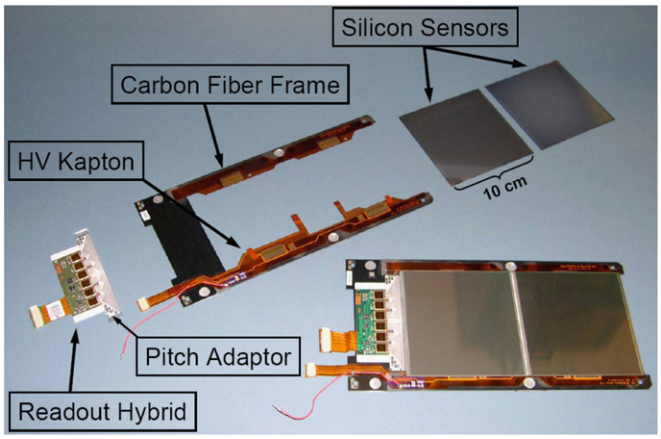


**Fig. 16.** A CMS module. The different parts forming a module are the frame of carbon fiber and Kapton; the hybrid with the front-end electronics and pitch adapter and the silicon sensors. [Courtesy of colleagues from UCSB Santa Barbara, California.]

All modules were fabricated in a robotic assembly line. The only differences among the modules are sensor orientation, one or two sensors, and four or six front-end chips. The large volume and numbers of components no longer allow the placement of the hybrid outside the sensitive volume. Fig 17 represents a schematic view of a CMS pixel module populating the three inner silicon tracking layers of the CMS detector. With the pixelated structures, the chip covers the full sensor, and a electronic to sensor channel connection is realized via bump bonding—see also Fig. 7.

### 1.5. Large systems, basic strategies

The modules are directly mounted either on the support structure (see Sections 2.2 and 2.3) or in the CMS case, to larger substructures like rods or petals (see Section 2.4). Numerous geometrical arrangements exist, mainly forward walls in fixed-target experiments or barrel structures, often with complementary forward wheels in the collider experiment to cover a maximum $\eta$-range. The purpose is to measure precise tracks of charged particles in a magnetic field. Initially, silicon trackers only complemented the more distant gas tracking detectors.

In the end, tracks allow

- the measurement of the particle' momentum $p_T$ or $p_\perp$:
  - thus also the measurement of energy;
- the identification of second and tertiary vertices;
- isolation of several particles with track close to each other.

The $p_\perp$ resolution and the impact parameter resolution $\sigma_{d_0}$, the parameter to identify secondary vertices, impose strong design criteria on any tracking device.

$p_\perp$ *resolution*: The transverse momentum resolution $p_\perp$ is defined by

$$\frac{\Delta p_\perp}{p_\perp}\approx\frac{\Delta s[\mu m]}{(L[cm])^2 B[T]}p_\perp\ [GeV] \tag{13}$$

with sagitta $s=L^2/8R$, lever arm $L$, magnetic field $B$, curvature radius $R$ and momentum $p_\perp$. The equation immediately shows that (1) intrinsic position resolution has to be good to resolve $s$ and that (2) the B field strength gives a linear improvement, while (3) a larger lever arm improves momentum resolution quadratically. An explanatory scheme is given in Fig. 18. With increasing $p_\perp$, the resolution gets worse again, and with an error of 100%, not even the charge of the particle can be identified anymore. The superior

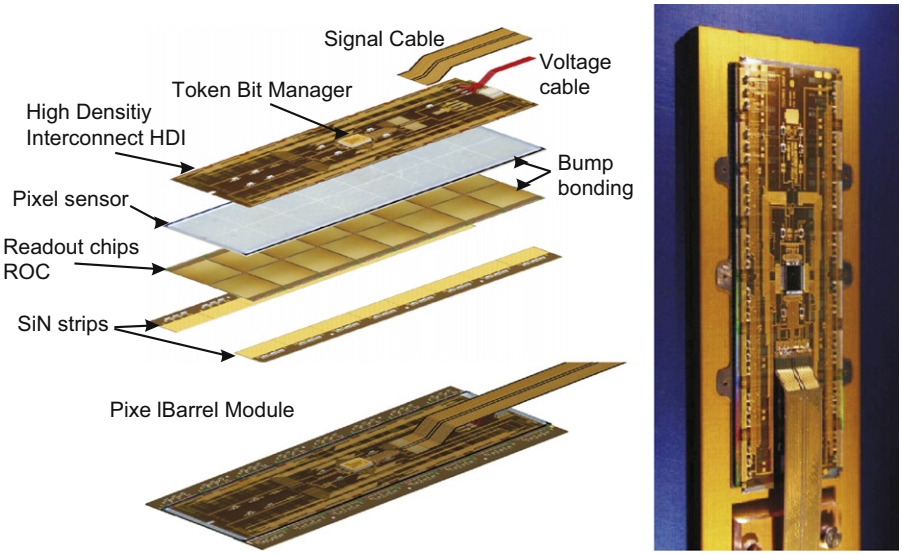


**Fig. 17.** Pixel module—barrel type [30].

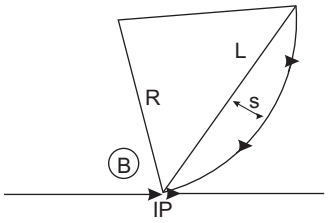


**Fig. 18.** Transverse momentum resolution $p_\perp$. The momentum resolution of a moving charged particle in a B field is given by its curvature path. With $s=L^2/8R$ and $B\cdot R=p/q$ one obtains the momentum resolution as $\Delta p/p\approx(\Delta s/L^2B)p$.

point resolution of silicon sensors with respect to wire chambers clearly improves the impact parameter on the other hand, the lower lever arm in the LEP experiments requires more outer gas tracking detectors. The early vertex detectors were more track seeders and vertex finders than full tracking detectors. This situation changed with the CDF II upgrade and the current LHC detectors. Today, silicon trackers dominate the muon momentum resolution and are augmented only above several hundred MeV by the large lever arm of the outer muon detectors. They are superior to the outer calorimeters in energy resolution for lower energies.[10]

*Impact parameter resolution* $\sigma_{d_0}$: The real strength of silicon tracking devices comes with the ability to identify short-lived heavy flavor quarks, which decay soon after their production and even before they reach any detector material. The high precision allows a decent track extrapolation down to the decay vertices. In Fig. 19, a DELPHI b quark event is displayed. The precise measurement of the vertices allows a determination of the flight path proportional to the particle lifetime and vice versa, and known-lifetime/flight path length quarks can be identified/tagged. The ability to reconstruct or detect secondary vertices can also be expressed by the *impact parameter resolution* $\sigma_{d_0}$. The impact parameter $d_0$ is defined by the shortest distance between a reconstructed track and the primary vertex. It is a crucial quality parameter of the full detector performance. If the measured *i*mpact *p*arameter IP is significantly larger[11] than the experimental resolution in this quantity, a secondary decay vertex is probably present. How the impact parameter is related to physics

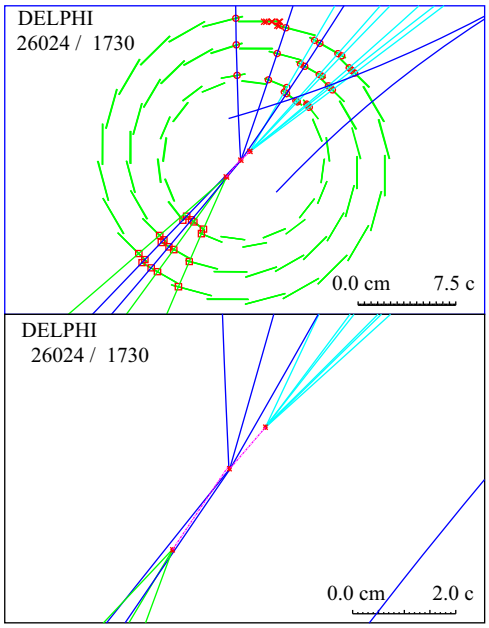


**Fig. 19.** A b-event with the DELPHI vertex detector. The upper part of the figure displays the different track points of the three detector planes together with the reconstructed tracks. The lower part, an exploded view, shows the capability of track interpolation down to the primary vertex and the capability to resolve the secondary b-vertex. This plot fully expresses the power of a micro-vertex detector to tag b quarks and determine the flight path of a short-lived particle. [Courtesy of DELPHI, CERN.]

will be discussed later; this section concentrates on the detector design aspects. The value $d_0$ is dependent on the detector geometry and strongly on multiple scattering, hence the material budget obstructing the flight path. For a simplified two layer system, the variance of $d_0$ can be expressed by

$$\sigma_{d_0}^2=\sigma_{MS}^2+\sigma_{geom}^2 \tag{14}$$

with

$$\sigma_{geom}^2=\left(\frac{\sigma_1 r_2}{r_2-r_1}\right)^2+\left(\frac{\sigma_2 r_1}{r_2-r_1}\right)^2 \quad \text{and} \quad \sigma_{MS}^2=\sum_{j=1}^{n_{scatt}}(R_j\Delta\Theta_j)^2 \tag{15}$$

[10] E.g., around 15 GeV in the case of CMS.
[11] The track does NOT pass through the primary vertex.

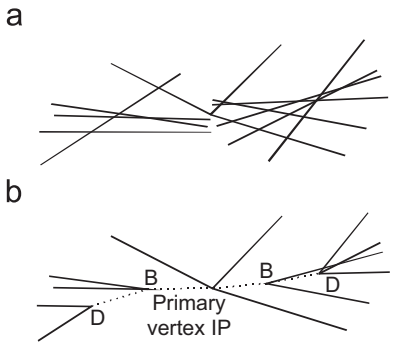


**Fig. 20.** A $b\bar{b}$ event, tracks and physics reconstruction. Two B mesons coming from the primary vertex are each decaying into a D meson, which shortly afterward decays into K mesons ($b \to c \to s$). Five tracks must be resolved in this "simple" scenario. One should remember that tracks in silicon or drift chambers are not continuous tracks as in bubble chambers. (a) The reconstructed tracks, shown using the space point coordinate information of the silicon detectors. (b) The fully reconstructed $b\bar{b}$ event, showing the two B mesons and their decay to D mesons. The different vertices are also reconstructed [16].

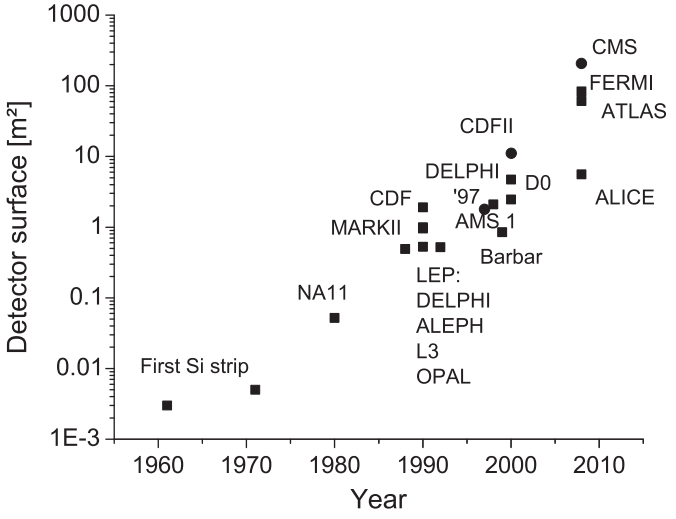


**Fig. 21.** The evolution and usage of silicon in high-energy physics detectors can be impressively shown by their increase in area during the last decades [5].

with $\sigma_1$ and $\sigma_2$ the intrinsic resolution in the measurement layers and $\Delta\Theta_j \simeq (0.0136/p_\perp^{beam}[\mathrm{GeV}/c])\sqrt{\Delta X/X_0}[1+0.038\cdot\ln(\Delta X_j/X_0)]$ the average multiple scattering angle of a particle with momentum $p_\perp^{beam}$ traversing through the material of thickness $\Delta X_j$ (expressed in fractions of a radiation length $X_0$) located at radius $R_j$ and $n_{scatt}$ the number of layers in front of the last detection element. The IP resolution is often parameterized by $\sigma_{d_0}^2 = \sigma_{asympt}^2 + (\sigma_{MS}/p_\perp)^2$ with $p_\perp$ in GeV/$c$ (a fitted value derived from detector operation).

All the above considerations lead to the following design goals:

- Low mass for beam pipe and vertex detector, including cables and support structures to minimize Coulomb Scattering (e.g., all electronic components were placed outside the detector volume). This priority is especially high in front of the very first measurement layer: Keeping $\Delta X_j/X_0$ and $\Theta_j$ small results in a small $\sigma_{MS}$.
- Placement of the first detection layer as close as possible to the primary interaction point to minimize extrapolation error, thus maximizing impact parameter resolution: $r_1$ small.
- Largest possible radius for the outer measurement layer: $r_2$ large.

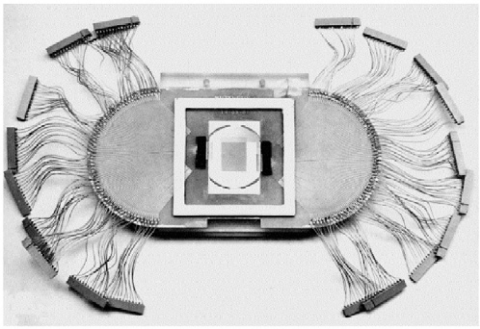

**Fig. 22.** Photograph of a mounted NA11 Detector [18]. The sensor seen in the center is $24 \times 36$ mm$^2$ in size with 1200 diode strips and readout of every 3rd (6th in the outer region) strip, resulting in 4.5 μm (7.9 μm) resolution. Relaxing the readout electronic connection density to 120 μm with a physical pitch of 60 μm is accomplished by connecting the even strips on one sensor side and the odd ones on the other.

- High intrinsic detector resolution, thus silicon sensors with small pitch and analog readout for hit interpolation in between strips: $\sigma_1$ and $\sigma_2$ small.
- Take alignment into account from the very beginning, thus overlap sensors to allow extrapolation of exact position with tracks crossing overlapped modules.
- Establish good algorithms for alignment, pattern recognition and vertex identification in the early stage.

In Fig. 20 a $b\bar{b}$ event shows what the real particle paths and the paths initially reconstructed from the space points look like. To understand the full decay cascade, all the vertices should be reconstructed. The situation becomes even more ambiguous once tracking imperfections and the effects of multiple scattering are introduced.

## 2. Silicon tracking systems of the last 30 years

Fig. 21 shows the development of systems in recent decades, and each system has its own design considerations and problems. All implementations follow the basic principles given in the previous section—light, close to the interaction point, large lever arm, excellent point resolution, track isolation, redundancy. Most of the current tracking devices deploy sensors fabricated by planar technology [18], similar to standard industrial integrated circuit fabrication. Smaller, earlier devices were made of standard CCDs, and silicon drift detectors are also in use in detectors installed in heavy ion colliders. In the following sections, the designs of NA11, DELPHI, CDF and CMS are described as examples.

### 2.1. NA11

NA11 was the first larger system exploiting high-precision silicon sensors to identify charm mesons and measure their lifetime and mass. The detectors are made of high-ohmic (3 kΩ cm) n-doped silicon single crystal wafers of 2 in. diameter and 280 μm thickness. Using the planar process, p-doped strip diodes covered by aluminum contacts (DC-coupled) are implanted into one side of the wafer. Fig. 22 shows a photo of the sensor, including the enormous connectivity needed at the time. The use was driven by the needs of

- Spatial resolution: better than 10 μm and good particle separation.
- Rate capability about $10^6$ Hz.
- Low multiple scattering and photon conversion—thin sensors.

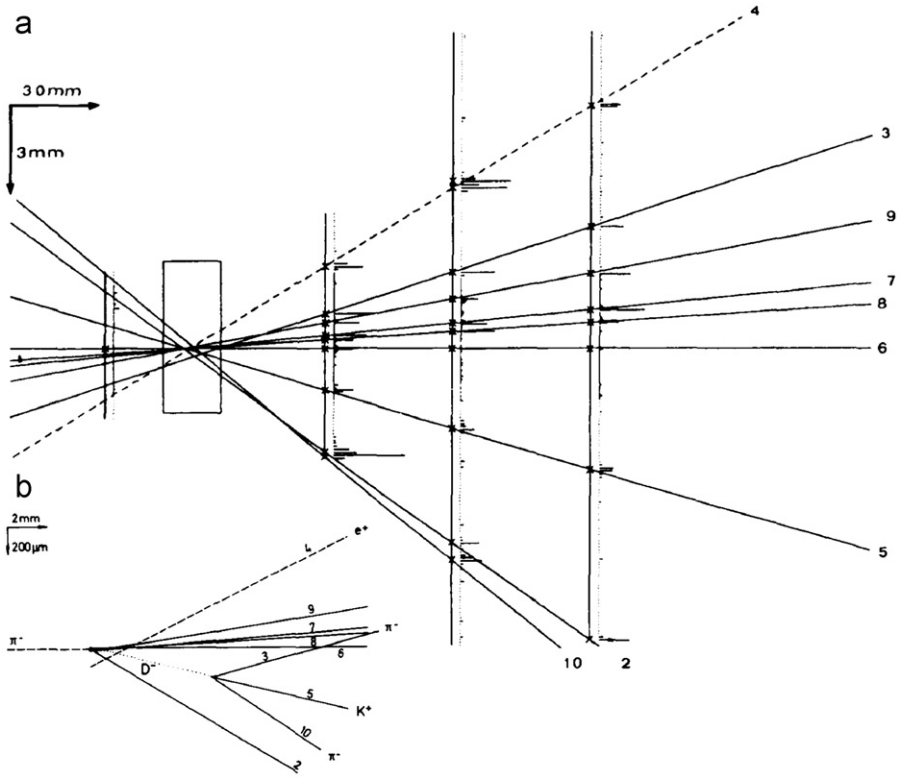


**Fig. 23.** Reconstruction of the production and decay of a $D^- \rightarrow K^+\pi^-\pi^-$ as measured in the NA11 experiment in 200 GeV/$c$ $\pi^-$Be Interactions [17]. The lengths of the horizontal lines on the planes indicate the measured pulse height in the silicon sensors. The connecting lines represent the reconstructed particle paths. With precise reconstruction, it becomes clear that trajectories 3, 5 and 10 are not originating from the same decay point as the others. They are not starting from the primary vertex, but from a secondary vertex. Distance reconstruction gives the boosted flight path $c\tau\gamma$ of the associated charm particle, which is directly correlated to its lifetime.

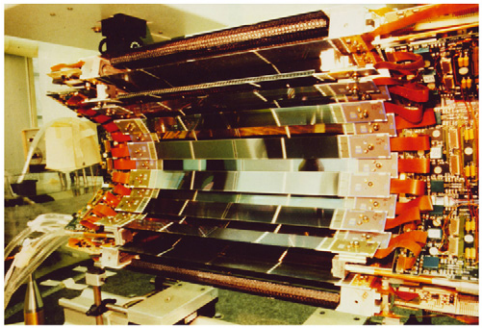

**Fig. 24.** The DELPHI silicon detector, view from within. After its first upgrade in the spring of 1994 the DELPHI *M*icro-*v*ertex *D*etector (MVD) was state of the art. The photo shows a rare view during construction, with all the modules in hand and three layers of the barrel detector assembled. Compared to LHC detectors, it was quite small. The modules were placed in a "staggered" arrangement in which the adjacent modules overlapped by a few strips, which allowed for tracks through neighboring sensors to be used for alignment and to make sure that the whole cylinder is covered.

An event display that also shows the full configuration is presented in Fig. 23. Eight silicon strip detectors (two in front and six behind the target) of the above described sensors were used in the NA11 spectrometer at CERN SPS. The detectors come in plane pairs with $\pm 14^\circ$ inclination with respect to the horizontal. The measurement is so precise that flight paths can be reconstructed and that secondary vertices can not only be identified but the flight path of the decaying particle from its production to its decay can be quantified. Finally, a handful out of several million recorded showed a charm decay. The measured distance between the primary and the secondary vertices gives the boosted flight path $c\tau\gamma$, which is directly correlated with the lifetime of the particle. The accuracy of vertex identification is 130 μm.

The configuration was suited only for a pure forward spectrometer and miniaturization of electronics; a larger silicon detector area would be needed for a detector in a collider environment. Additionally, a two-dimensional readout, by segmentation of both sensor faces, would clearly be beneficial. Nevertheless, NA11 was a fundamental milestone in the history of silicon tracking systems.

### 2.2. Detector with Lepton, Photon and Hadron Identification (DELPHI)

The Micro-Vertex-Detector (MVD) was situated in the heart of the DELPHI detector. Its mission was to reconstruct secondary and tertiary vertices and seed the tracks for the outer drift chambers. There was a clear bifurcation of tasks between the silicon and gaseous detectors. The MVD underwent several substantial upgrades, from single-sided to double-sided sensors and finally to the implementation of a forward structure, allowing tracking down to a polar angle of 10.5°. Starting in 1989, as the first silicon detector in the LEP experiment with two layers measuring the $\phi$ coordinate, it was upgraded to three layers[12] in 1990, while in 1994, double-sided[13] sensors were introduced to add the $z$-coordinate. An impressive view into the DELPHI MVD of 1994 is shown in Fig. 24.

[12] Size reduction of the beam pipe allowed an additional layer at smaller radius.

[13] DELPHI followed the example of ALEPH, which started immediately with double-sided silicon sensors.

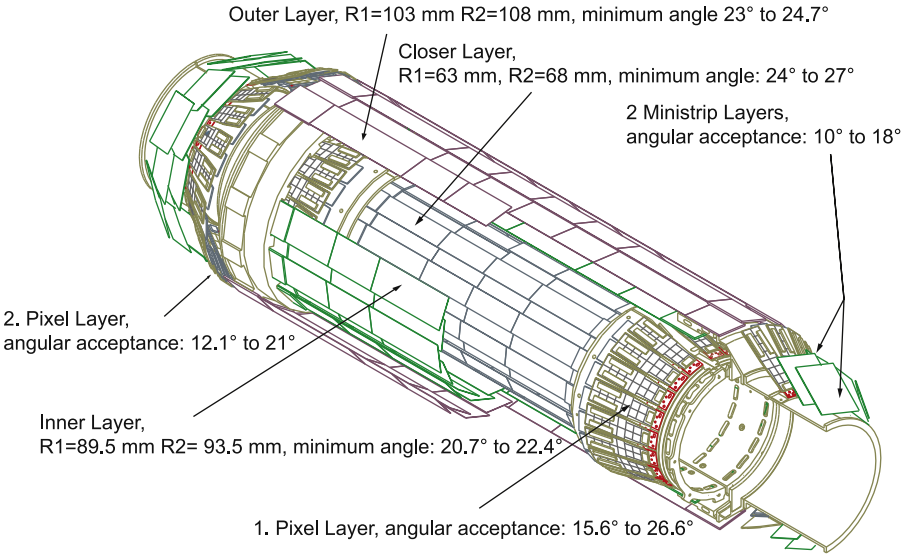


**Fig. 25.** The DELPHI micro-vertex detector [19].

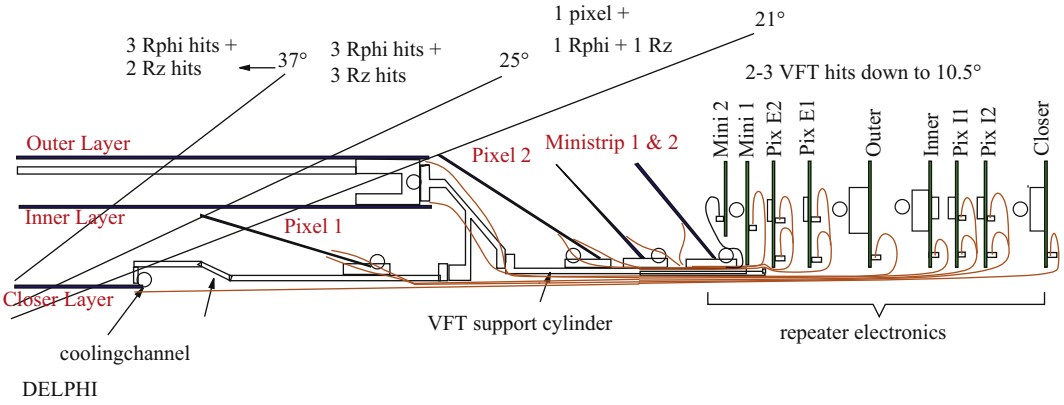


**Fig. 26.** Cross-section of the DELPHI tracker—a novelty for a collider vertex detector, a forward part. DELPHI pioneered the field in two ways: (1) forward tracking and (2) use of hybrid-pixel sensors. To cope with the tight space constraints, quadratic strip sensors were mounted back-to-back with the electronics hybrid glued on top of the sensors on both sides. A single type of sensor geometry was used—the ministrip sensor, a $53 \times 53$ cm$^2$ quadratic single-sided sensor. Towards the center, DELPHI uses the new pixel technology to establish good pattern recognition with an intrinsic 2D readout. Thin, long pixel modules just fit in this crowded region. The pixel modules reach fully into the barrel strip region [19].

The final constellation, installed in 1997, is shown in Fig. 25. DELPHI pioneered the use of hybrid pixel detectors and a forward instrumented section.[14]

The main goal of the last upgrade was to increase hermeticity and expand the b-tagging capabilities. These goals are met by extending the barrel region to achieve b-tagging capability down to 25° and active sensor area down to 10.5° with the additional pixel and ministrip sensors. The three layers also help to solve possible track ambiguities. The entire structure is 85 cm long and has 1.5 m$^2$ of active silicon sensors. A schematic of the DELPHI double-sided sensor is shown in Fig. 5 in Section 1.2.

*DELPHI MVD barrel part*: The DELPHI MVD is divided into Closer at $R=6.6$ cm, Inner at $R=9.2$ cm and Outer Layers at $R=10.6$ cm, fitting tightly between the beam pipe and the inner drift chamber. The *smallness* of the detector allows for many fancy solutions and very distinct optimizations. The basic concept is the use of double-sided sensors in the Closer and Inner layers and back-to-back modules in the Outer layers, where the Coulomb scattering is less critical. The front-end hybrids reside at the end, equipped with MX6 chips serving two sensors each in the Closer layer and two or four sensors in the Inner layer. In the Outer layer one hybrid serves four sensors with the newly developed Triplex chip, optimized for larger capacitances. All hybrids are double sided, with chips on both sides. In the $R\Phi$ plane, the point resolution is around 8 μm, and it is between 10 and 25 μm in the $Rz$ plane, varying for different track inclinations. Throughout the tracker, great emphasis was placed on the overlap of sensitive silicon within each layer to allow for self-alignment procedures—a staggered design, see Fig. 24. The Closer layer is 36 cm long, while the Inner and Outer barrels are 55.5 and 55.9 cm in length. The bulkhead is constructed of aluminum but all internal structures are lightweight Kevlar plus carbon fiber only. The meticulously designed concept pays off and results in $\sigma^2_{p_\perp} = 28^2 + (71/p_\perp)^2$ for $R\Phi$ and $34^2 + (69/p_\perp)^2$ for $RZ$.

*DELPHI MVD forward part*: A detailed schematic cross-section can be seen in Fig. 26. Schematic Fig. 26 shows in detail, which detector component is active in each of the different polar angle regions.

The forward region is equipped with hybrid pixel detectors and rectangular strip detectors, called ministrips. Pixel and ministrip modules are displayed in Fig. 27.

A ministrip detector consists of 48 modules arranged in two layers on the MVD bulkheads. Every detector is quadratic $5.3 \times 5.3$ cm$^2$; therefore, two single-sided sensors can be

[14] They are necessary to improve track extrapolation towards the forward Ring Imagine Cherenkov Counter, (-RICH) to improve *P*article *Id*entification (PID).

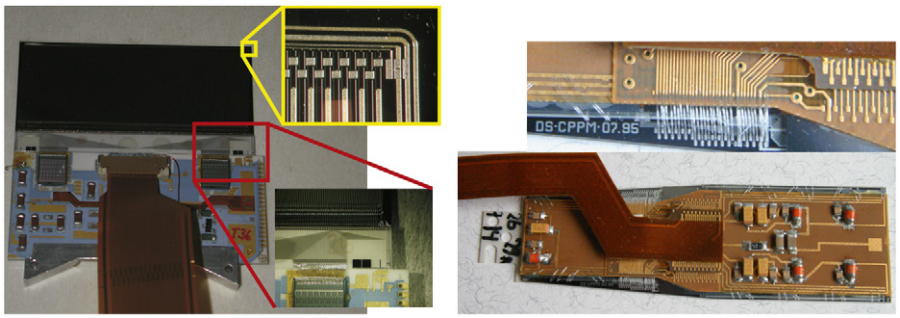


**Fig. 27.** A DELPHI ministrip and pixel module. The left picture shows one side of a ministrip sensor module. The hybrid-to-sensor wire-bonding took place in the middle of the sensor. The sensor itself is biased via FOXFET. The FOXFET ring layout is shown in the exploded view of the sensor corner. The guard ring was connected to ground. A second zoom shows the hybrid edge, including the chip edge. The right picture shows a complete pixel module. The sensor-chip sandwich (bump-bonded) is covered by a Kapton flex structure, carrying the necessary passive components and the bus lines. The exploded view shows the wire-bonding from pixel chip bus lines to Kapton bus lines [20].

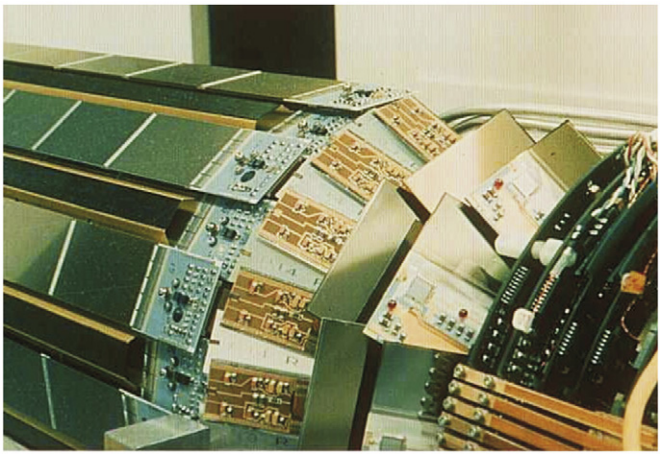

**Fig. 28.** The very forward part of the DELPHI tracker. The photo shows the forward pixel and ministrip detector. At the time of design and construction these innovative parts enabled tracking down to $\Theta = 9^\circ$. [Courtesy of DELPHI, CERN.]

mounted back to back at a 90° angle to establish an intrinsic 2D readout. The hybrids are glued directly onto the sensor serving 256 strips. The strips are arranged with a stereo angle of 2°. Due to Coulomb scattering and to unavoidable material (e.g., hybrids from the barrel modules) the resolution is limited to about 100 μm, and the readout pitch can be relaxed to 200 μm with one intermediate strip. The stereo angle helps to resolve track ambiguities in the crowded forward direction. Modules of ministrip layer 1 are placed in reverse[15] with respect to layer 2, with a resulting effective angle of 4° between strips. Two particle tracks hitting the same coordinates in one plane now hit, by construction, different coordinates in the second "tilted" plane.

The pixel detector is formed of 152 modules. A pixel intrinsically has a 2D readout and is therefore predestined to have a marvelous pattern recognition capability, reducing any ambiguity. The modules are inclined, as seen in Fig. 26. Each pixel module area contains 8064 pixels with a size of $320 \times 320\ \mu m^2$. Unlike the strip sensors (described in the next section), the pixel sensors are DC-coupled, and one module is readout by 16 separate chips, which are the same size as the pixels of the silicon sensors.

Fig. 28 concludes the DELPHI section with a photo of the forward region of the MVD.

### 2.3. Colliding detector at Fermilab CDF

The TEVATRON, a proton anti-proton collider, has operated since 1987 at the Fermi National Laboratory near Chicago, complementary to the electron–positron collider LEP at CERN. A first CDF proposal of a silicon vertex detector to improve tracking resolution and to allow the tagging of heavy quarks was written up in 1985 [21]. The CDF experiment finally deployed the first silicon detector in a hadron collider environment in 1992: a two-barrel, four-layer detector, assembled of single-sided DC-coupled sensors and non-radiation-tolerant integrated circuits—the SVX. The concept of a tracking device at a small radius at a hadron collider was questionable at first; many believed it would be completely (100%) occupied. The SVX was replaced in 1993 by the SVX' with a similar geometry but advanced sensor and electronics technology. A peculiarity is the consequent realization of the wedge geometry for the inner SVX detectors, resulting in the use of dedicated sensors with a different width for every layer. The detectors' main task was the identification of secondary vertices and track seeding for the outer tracking drift chamber.

It should be mentioned that claiming the top discovery would have been very difficult without the reconstruction of the beauty quarks by the silicon vertex detector.

Design criteria were similar to the LEP experiments, but additional aspects were also important:

- To obtain the best impact parameter resolution, a high precision point was needed as close as possible to the interaction point, together with a precision link space point or a better track segment to the outer drift chamber.[16]
- In contrast to the LEP experiments in the TEVATRON, a hadron collider, the interaction region is longitudinally stretched with a $\sigma_Z$ of 35 cm. It thus requires a long detector to cover as much as possible of the interaction.
- Reducing multiple scattering to the bare minimum, as the material budget must be minimized.
- The internal mechanical tolerances must match the intrinsic detector resolution, i.e., about 10 μm, while the accurate placement with respect to the outer detector must match the resolution of the surrounding drift chamber.
- (for the RUN II upgrade) The use as a deadtimeless level 2 trigger imposed additional constraints:
  - The wedge geometry—compatible with hardware regional track reconstruction.
  - The very tight mechanical tolerances—no alignment tweaks allowed in the trigger.
  - The readout chip—onboard digitization, sparsification, and buffering.

[15] The "horizontal" planes face each other; therefore strips are oriented $\pm 2^\circ$.

[16] CTC *C*entral *T*racker *C*hamber for RUN I and COT *C*entral *O*uter *T*racker for RUN II.

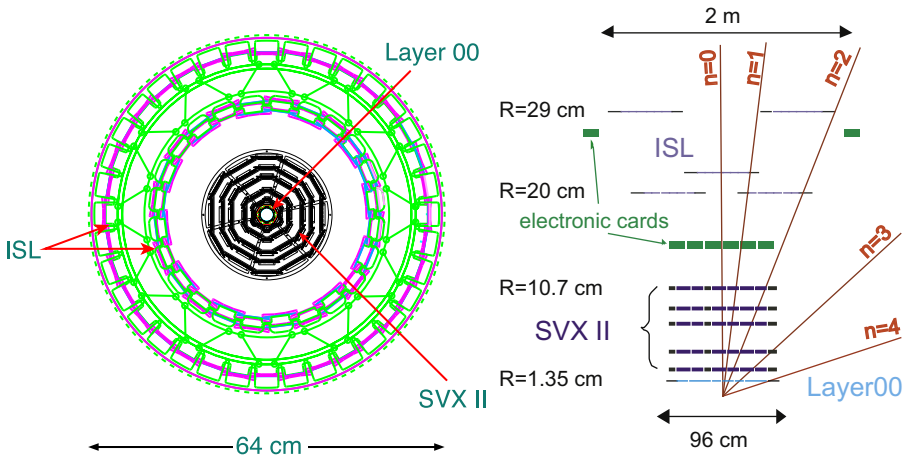


**Fig. 29.** The schematic of the CDF silicon tracking system. The end view (left) clearly shows the wedge shape of the five inner SVX 2 layers. The more outer spaced ISL detectors link the silicon tracking to the outer drift chamber. The $z$-view (right) displays the consequent "outside" placement of the electronic components to minimize multiple scattering. The long length of 2 m is necessary to cover $|\eta| \leq 2$ without forward instrumentation [22].

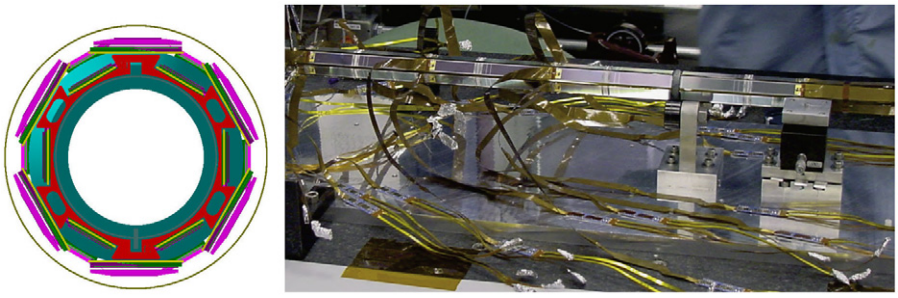

**Fig. 30.** End view of the Layer 00 detector and a rare view during assembly. The left side shows the tightness, allowing only 0.8 cm (1.5 cm) wide sensors at a radius of 1.35 cm (1.6 cm). Layer 0 of the SVX II detector sits at $R=2.45$ cm. On the right, Layer 00 is visible with silicon sensors not yet covered by the thin long fine-pitch cables. The main importance of Layer 00 is the first high-precision space point at very low radius to seed the impact parameter calculation before multiple scattering [23].

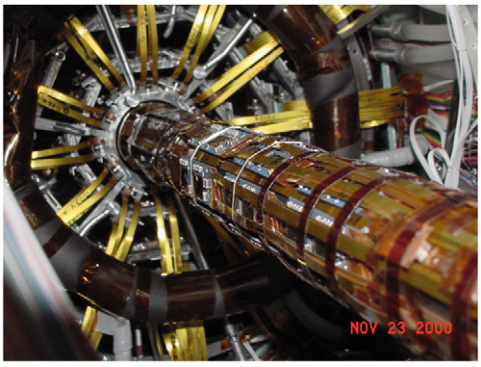


**Fig. 31.** Layer 00 during insertion. The clearance towards the SVX II detector is only about 300 μm. Insertion finally succeeded in November 2000 [23].

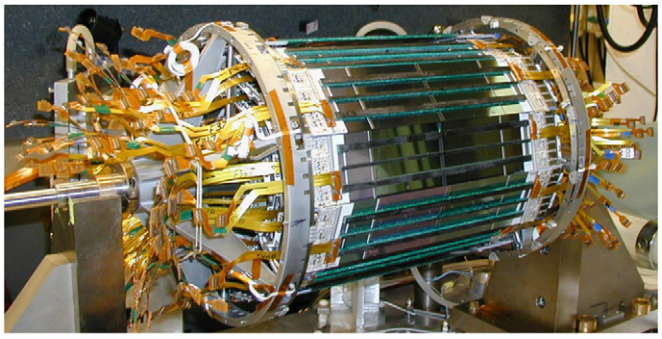

**Fig. 32.** The SVX II detector, one barrel. [Courtesy of CDF, Fermilab.]

- Special considerations in the readout and trigger electronics chain.

### 2.3.1. The CDF silicon detector at RUN II

This section concentrates on the last upgrade – L00 + SVX II + ISL[17] – for RUN II, which started in 2000, although most design criteria are valid for all detector stages. The tracking system was largely increased for the RUN II upgrade; the silicon barrel detector's length was increased to almost 2 m to cover a pseudo-rapidity[18] $|\eta| \leq 2$ without any endcap structure. The schematic is displayed in Fig. 29.

Efficient precision charged-particle tracking is extremely important for the CDF analysis technique. Reconstruction of both high $p_\perp$ ($m_W$) and low $p_\perp$ ($B \rightarrow J/\Psi K$) is required. The combination of track, calorimeter and muon chamber information, with excellent purity at both the trigger and offline level, is possible. Precise and efficient b-tagging is essential for top physics and new phenomena searches. The goal is to guarantee precise 3D impact parameter

[17] Layer 00, Silicon Vertex Detector II and Intermediate Silicon Layers.

[18] Pseudo-rapidity $\eta = -\ln(\tan \Theta/2)$ replaces the azimuthal angle $\Theta$ and is invariant vs. Lorentz addition. In hadron colliders the $z$-coordinate of the primary vertex varies. Therefore, the quantity $\eta$ is used in calculations but also to define and construct the detector elements.

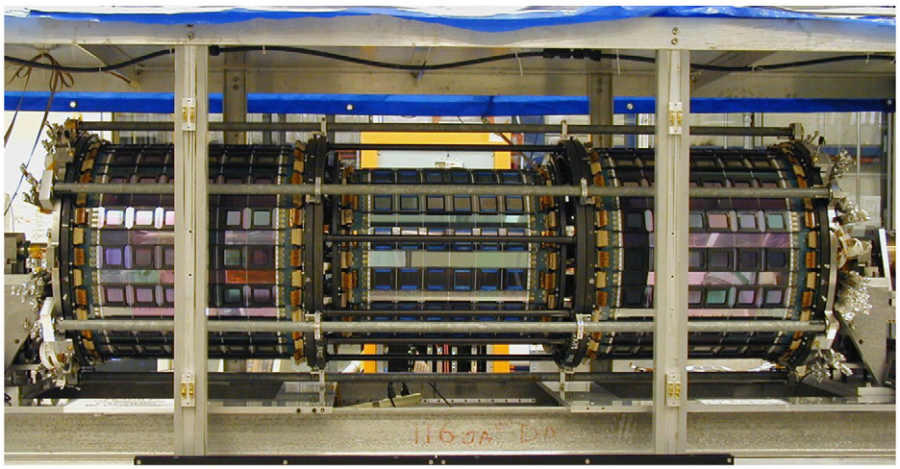

**Fig. 33.** The intermediate silicon layers detector. [Courtesy of CDF, Fermilab.]

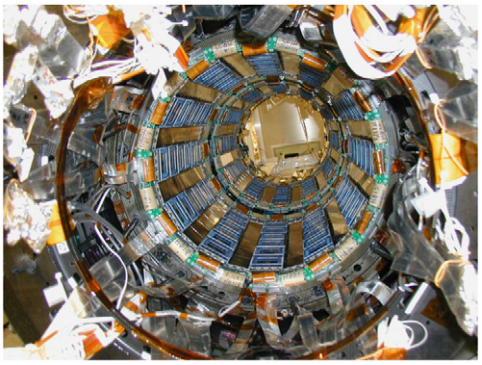

**Fig. 34.** Into the ISL. The full ladders, six sensors long with readout electronics on both sides, are visible in a barrel configuration, a rare view during construction. [Courtesy of CDF, Fermilab.]

resolution with an enhanced coverage up to $|\eta| \leq 2$. The CDF II tracking system consists of an inner silicon vertex tracking system and a large drift chamber. The inner tracker consists of a minimum radius inner layer (Layer 00 at 1.35 cm), glued to the beam pipe and a five layer silicon detector (SVX II at $R$=2.7–10.7 cm, spanning a length of $\sim$1 m) with two-dimensional readout in each layer. It is surrounded by a third two-layer silicon detector (ISL $R$=20 and 28 cm) and finally an eight-layer open cell drift chamber (*C*entral *O*uter *T*racker COT at $R$=44–132 cm). The close schematic and a photo of L00 is displayed in Figs. 30 and 31. The SVX II can be seen in Fig. 32, while the ISL is shown in Figs. 33 and 34.

The inner and outer tracking systems are capable of stand-alone tracking, which enables track–track matching instead of the normal track-space point fit. The COT gives Level-1 trigger information and the inner silicon tracking system provides Level-2 information. The trigger acts on displaced vertices. The realization of this object, with a size about one order of magnitude larger than DELPHI, was a real challenge. It must be mentioned that the CDF detector bridges the LEP and LHC detector concepts: the larger, outer ISL detector is constructed more like an LHC detector, with large sub-structures (modules) and only two sensor types placed on a large modular spaceframe, while the inner L00 and SVX II make use of different sensors and even sensor technology for the individual layers.

*Layer*00—*L*00: *L*00 [24] makes use of radiation-hard, high-voltage robust sensor technology concepts developed for the LHC. A six-wedge layer is mounted directly on the beryllium beam pipe with single sided silicon microstrip sensors, each 7.8 cm long and 0.8 cm or 1.5 cm wide. The length of Layer 00 is approximately 94 cm, consisting of six modules with two sensors per module, for a total of 144 sensors. The outer placement (routed by fine pitch cables) of the electronics (see Fig. 30) reduces the material budget but also moves them out of the high radiation environment.

*Silicon Vertex Detector II—SVX II*: The SVX II utilizes double-sided sensors with partially double metal layers and each layer having individual geometry.

The SVX II is divided into 12 wedges in $R\phi$ and into three barrels in $z$ (beam axis) with a length of 29 cm each. With a length of almost 1 m, SVX II covers $\approx 2.5\sigma$ of the interaction region, providing track information up to $|\eta| \leq 2$. It has five double-sided silicon layers measuring the $R\phi$ and $Rz$ coordinates. Three layers (0, 1 and 3) have a 90° stereo angle, allowing high-resolution $Rz$ measurements, while layers 2 and 4 have a 1.2° stereo angle. This design provides good pattern recognition and 3D vertex reconstruction with an impact parameter resolution $\sigma_\phi < 30\,\mu$m and $\sigma_z < 60\,\mu$m for central high momentum tracks. A photo of one SVX II barrel is displayed in Fig. 32. Half-ladders contain two sensors plus a hybrid mounted directly to the silicon surface at the end. Two half-ladders are daisy-chained together to form full ladders of four sensors each. A total of 720 sensors form either 360 half-ladders or 180 full ladders. A 12-fold $\phi$ symmetry makes it possible to treat each 30° wedge as an independent tracker.

The 90° strips were routed to the module end by a dedicated double metal layer. Many sensors have been processed, for the first time in a HEP experiment, on 6 in. wafers.

*Intermediate Silicon Layers—ISL*: The Intermediate Silicon Layers 5 and 6, both consisting of double-sided silicon strip detectors, measure both the $R\phi$ and $Rz$ coordinates. The strips on one side of the wafers are parallel to the beam axis ($z$-axis), while the strips on the other side are tilted by 1.2°, which allows the measurement of the $Rz$ coordinate with low ambiguity[19] and no additional double metal layer. The ISL layers are mounted at the radii of 20 cm and 28 cm. The overall length of the ISL is 195 cm, covering the pseudo-rapidity region $|\eta| \leq 2$. This special long configuration enables "forward" tracking without forward structures. The ISL is presented in Figs. 33 and 34.

In contrast to SVX II, the ISL was designed with simplicity in mind. A more detailed description of the ISL can be found in Refs. [25–27]. The ISL sensors are also AC-coupled, polysilicon biased and double sided, with p+ stop configuration on the n-side. For the larger radii, occupancy and radiation damage is lower. It is

[19] The angle of 1.2° allows the connection of strips of several consecutive sensors to one single electronic readout channel, as opposed to layers with a stereo angle of 90° where multiple strips are connected to one routing line and hence to one readout channel.

therefore possible to use longer strips, and pitches are relaxed to 112 μm on the $R\phi$ and stereo side. The ISL ladders are composed of six sensors arranged as half-ladders of three sensors each with a double-sided hybrid at each half-ladder end. The 296 half-ladders form 148 full ladders, for a total of 888 sensors with 2368 chips.

*Silicon Vertex Trigger—SVT*: The ability to use impact parameter information in the trigger to detect secondary vertices can substantially increase the physics reach of a hadron collider experiment. Background can be quite substantially reduced, e.g., for the process $Z \longrightarrow b\bar{b}$. The B-decay and other studies will also be greatly enhanced. To obtain impact parameter information at Level-2, the silicon tracker is read out after each Level-1 trigger. The SVT combines data with the Level-1 tracking information from the COT and computes track parameters ($\phi$,$p_\perp$, and impact parameter $d_0$) with a resolution and efficiency comparable to full offline analysis [28,29]. The SVT also introduced several hard constraints, mentioned earlier, on the detector design and assembly.

### 2.4. Compact Muon Solenoid (CMS)—tracker

The design goal of the tracker is to operate with a maximum of 1% occupancy at all layers and a good impact parameter resolution in $R\phi$ and $Rz$ plus a large $\eta$ coverage. The detector is fully described in Refs. [30–33]. The requirements are

- efficient and robust pattern recognition;
- fine granularity to resolve nearby tracks;
- fast response time to resolve bunch crossings;
- ability to reconstruct heavy objects translating to 1–2% $p_\perp$ resolution at $\sim 100$ GeV;
- ability to operate in a crowded environment at 10 cm from primary vertex;
- ability to tag b/τ through secondary vertices;
- reconstruction efficiency: 95% for hadronic isolated high $p_\perp$ tracks and 90% for high $p_\perp$ tracks inside jets;
- ability to operate in a very high-radiation environment;
- efficient and precise tracking in the pseudo-rapidity range $|\eta| \leq 2.5$.

The result is a smaller pixelated detector in the center with a large volume strip detector surrounding it. All in all, a cylinder of 2.5 m diameter and 5.4 m length is instrumented with 206 $m^2$ of active silicon detectors. The CMS tracker is composed of a pixel detector with three barrel layers and a silicon strip tracker with 10 barrel detection layers extending outwards to a radius of 1.1 m. Each system is completed by endcaps, which consist of two pixel disks in the pixel detector and three small plus nine large disks in the strip tracker on each side of the barrel, extending the acceptance of the tracker up to a pseudo-rapidity of $|\eta| \leq 2.5$. It should be mentioned that CMS has a silicon-only tracking, where the pixel (with a stand-alone tracking) is responsible for the vertexing and track seeding, while the outer strip tracker is responsible for the tracking with a larger lever arm.

The different sub-detector locations can be seen in Fig. 35, where a quarter section of the detector is presented. The basic design strategy to stay below 1% channel occupancy defined the sensor and module geometries at all given radii. To keep the occupancy at or below 1%, pixelated detectors have to be used at radii below 10 cm. For a pixel size of $100 \times 150\ \mu m^2$ in $R$ and $z$, respectively, which is driven by the desired impact parameter resolution, the occupancy is of the order $10^{-4}$ per pixel and LHC bunch crossing. With analog signal interpolation, a hit resolution of $10(R\phi) \times 20\ \mu m(Rz)$ can be achieved. The pixel detector provides three 3D space points up to $|\eta| \leq 2.5$. Three pixel barrel layers are located at radii 4.4, 7.3 and 10.2 cm. The pixel barrel is 53 cm long. Two pixel forward disks at $z = \pm 34.5$ and $z = \pm 46.5$ cm guarantee 3D space point coverage up to $|\eta| \leq 2.5$. The detector is instrumented with 768 pixel modules in the barrel plus 672 modules in the forward disks for a grand total of 66 million pixels. A pixel module including an assembly picture is shown in Fig. 17.

The CMS *S*ilicon *S*trip *T*racker (SST), spanning radii 20 cm $< r <$ 110 cm plus a substantial forward region, is subdivided into *T*racker *I*nner *B*arrel (TIB), *T*racker *I*nner *D*isk (TID), *T*racker *O*uter *B*arrel (TOB) and *T*racker *E*ndcap (TEC).

The TIB has four barrel layers assembled in shells. Layers 1 and 2 are double sided (DS). It is complemented by two disk-shaped forward detectors (TID), each composed of three small disks. The TIB/TID spans the radii 20 cm $< r <$ 55 cm with a length of 2.2 m ($z < |110$ cm$|$). The TIB alone is 1.4 m long ($z < |65$ cm$|$). All modules are mounted on "strings", which are directly and individually placed on the structures. The reduced particle flux density allows the use of strip sensors with a typical cell size of 10 cm × 80 μm and 10 cm × 120 μm, resulting in an occupancy of up to 2–3% per strip and LHC bunch crossing. Modules are limited to one single sensor to accommodate the maximum strip length. The TIB and TID detectors are displayed in Figs. 36 and 37.

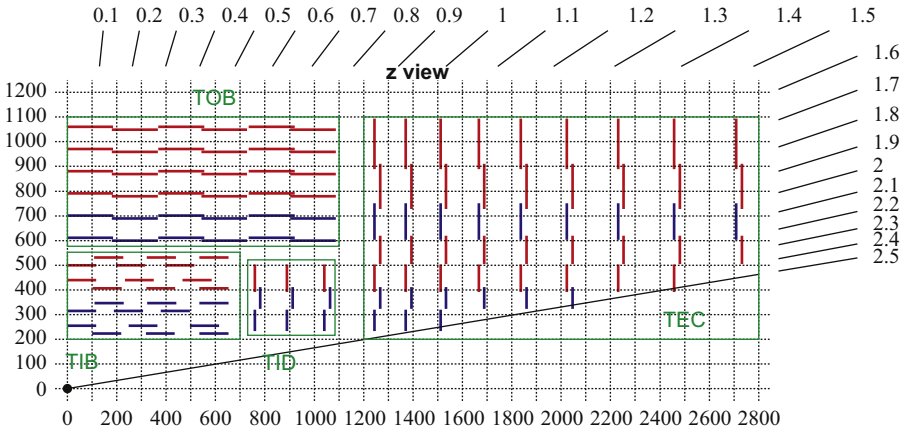


**Fig. 35.** The CMS strip tracker layout. At intermediate radii (20 cm $< r <$ 55 cm) the reduced particle flux allows the use of silicon micro-strip detectors with a typical cell size of 10 cm × 80 μm, resulting in an occupancy of up to 2–3% per strip and LHC bunch crossing. In the outer region (55 cm $< r <$ 110 cm) the strip pitch and length can be further increased for a cell size of 20 cm × 180 μm. The detector is consequently instrumented with barrel geometry (*TIB* and *TOB*), including some stereo modules, complemented with the forward inner disks (TID) and the large endcaps on both sides (TEC). Barrel Layers 1, 2, 5, 6, TID rings 1,2 and TEC rings 1, 2 and 5 are instrumented with stereo double-sided modules; the modules are colored blued. (For interpretation of the references to color in this figure legend, the reader is referred to the web version of this article.)

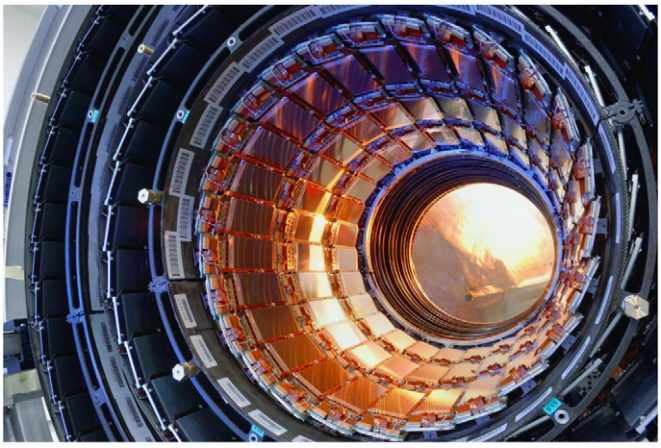

**Fig. 36.** *T*racker *I*nner *B*arrel (TIB). Three layers of the Tracker Inner Barrel detector are visible. Eventually, it will house the pixel detector. In the background, the inner edges of the three *T*racker *I*nner *D*iscs can be seen. [Courtesy of CERN.]

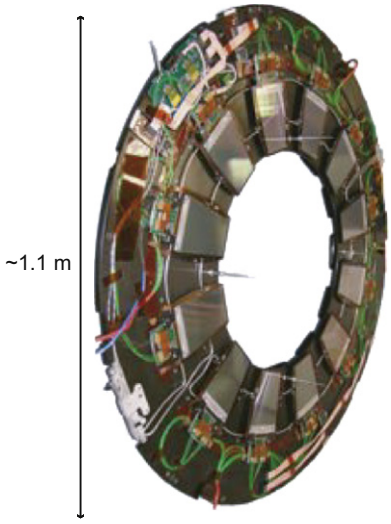


**Fig. 37.** One disk of the *T*racker *I*nner *D*isk (TID). Three of these disks on both TIB sides complete the inner detector fully embedded in the TOB [34].

The TOB structure where the modules are assembled in six concentric layers (layers 5 and 6 are DS) surrounds the TIB. It is located inside the electromagnetic calorimeter. The TOB spans radii of $55\ \text{cm} < r < 110\ \text{cm}$ and a length of 2.2 m ($z < |110\ \text{cm}|$). For a detector the size of the TOB, an individual module placement is no longer practical. A structure was designed where 688 one-meter-long "rods" equipped with modules are inserted. At these radii, the pitches and strip lengths can be increased, which helps to moderate the number of readout channels, given the large area. The cell size is $20\ \text{cm} \times 120\ \mu\text{m}$ and $20\ \text{cm} \times 180\ \mu\text{m}$ with two sensors daisy chained to one readout hybrid. The daisy chaining has obvious advantages but also increases the channel capacitance load and thus the noise. This problem is compensated by increasing the thickness from 320 μm (thin) for TIB/TID to 500 μm (thick) for TOB sensors. The same argument and design holds for TEC, where inner rings 1–4 are "thin" and ring 5–7 sensors are "thick". An important detail is the smaller pitch in the two outermost layers, reflecting the need to have a precision space point at a large lever arm and a precision link point to the calorimeters. For TIB and TOB, which have a barrel-like structure, the sensors are rectangular, and the strips run parallel to the beam (*z*-axis). A double-sided module is composed of two single-sided sensors mounted back to back, where one is tilted by an angle of 100 mrad with respect to the *z*-axis. A photo of the TOB and a rod can be seen in Fig. 38.

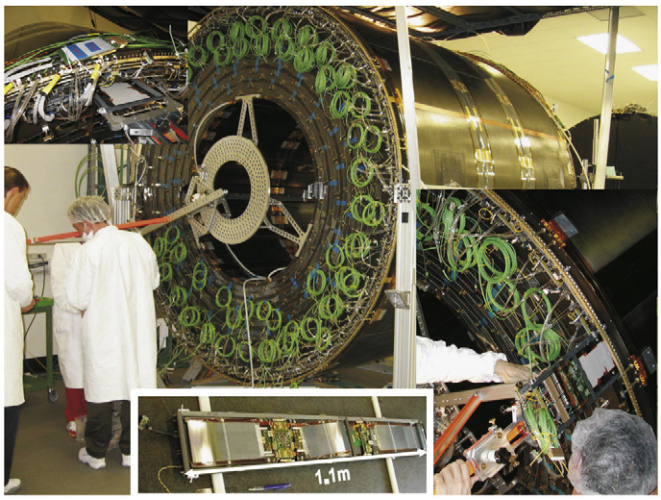


**Fig. 38.** Rod insertion into TOB. The main picture gives a good overview of the size and complexity of the TOB. A special tool guarantees a safe insertion. A rod is displayed at the bottom [33].

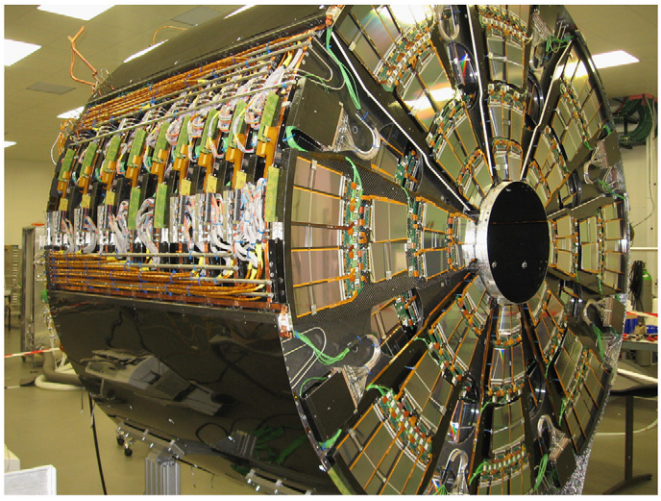

**Fig. 39.** The Tracker Endcap (TEC), fully equipped and open, a rare view. Eight petals are visible on the front. The space in between is covered with petals on the other non-visible side of the disk. Nine similar disks form one Tracker Endcap. The 96 visible wedge-shaped sensor modules placed in a wedge-geometry on the petals guarantee a continuous radial strip orientation. On the left, an opening shows all the services for one sector, out of eight. The diameter of one TEC is 2.5 m, while the length stretches to 1.7 m. One TEC holds 144 petals. All electrical and optical cables and cooling pipes were installed in autumn of 2005. Both TECs were fully ready, with all petals installed and inserted into the tracker support tube, in early 2007.

Two Tracker Endcaps (TEC) ensure a pseudo-rapidity coverage of $|\eta| \leq 2.5$. The strip orientation is radial, to achieve a continuity of all strips running radially through all rings from ring 1 to ring 7 sensors at different radii. Seven different types are necessary. All sensors are wedge type, and the outer pitches of, e.g., sensor W5A must match the inner strip pitches of sensor W5B. The detectors of rings 1, 2 and 5 are made of double-sided modules. Modules of rings 1–4 contain a single sensor, while rings 5–7 have a larger pitch and two sensors daisy chained together. As for the TOB, the modules are arranged on substructures—on wedge-shaped "petals". Petals hold up to seven rings of modules with the different geometries. One TEC consists of nine disks populated with petals, each covering 1/16 of 2 $\pi$. There are eight different petal types varying in radial length, hence the

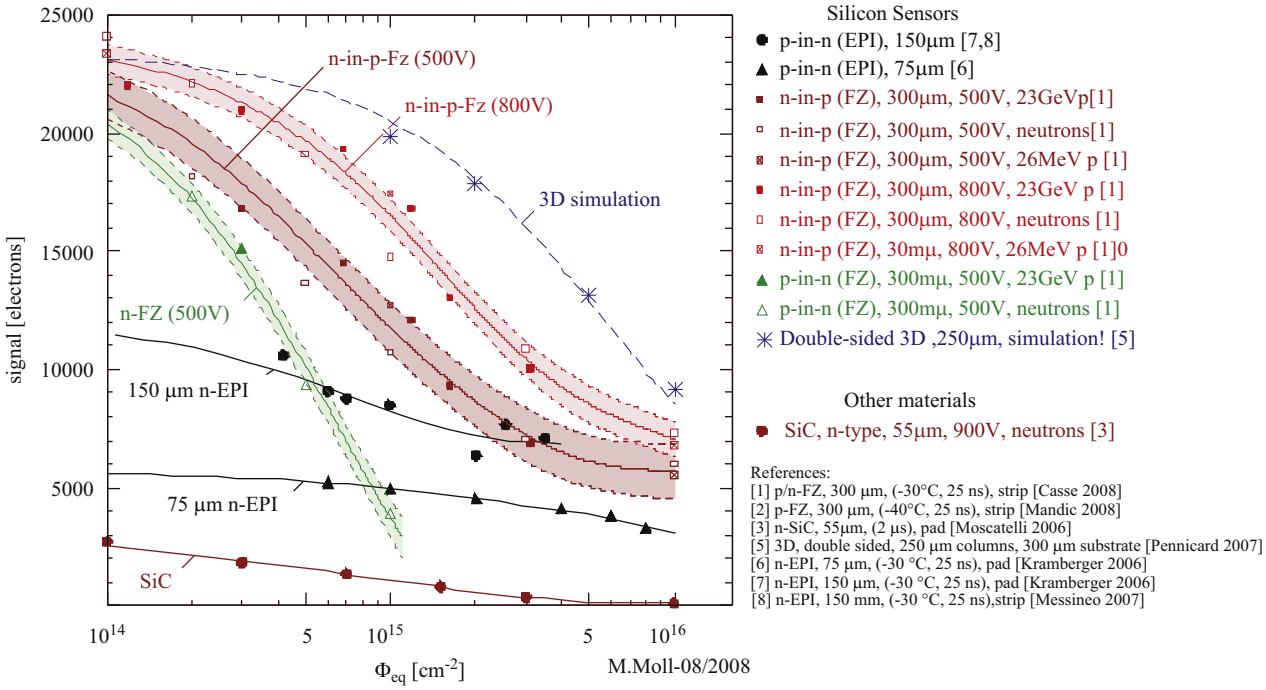


**Fig. 40.** The plot compiles possible signals for different materials and different sensor schemes (planar, 3D) vs. fluences. (Note: Measured partly under different conditions! Lines to guide the eye—no modeling!) [39].

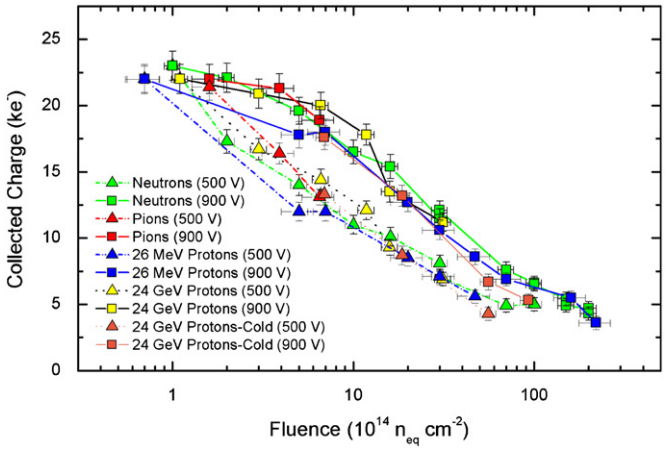


**Fig. 41.** The plot shows CCE for n-in-p FZ strip detectors vs. fluence of different particles. At high fluences trapping becomes the dominant factor and damage becomes almost particle independent. The knee in the rightmost tail even looks a bit too high and could be a hint toward charge amplification [41].

number of populated rings, to adapt for the location in $z$. Petal types differ for disks 1 and 2, 3–6, 7 and 8 and 9; the arrangement can be seen in Fig. 35. A total of 288 petals form both endcaps. The detector spans 120 cm $< |z| <$ 280 cm and 20 cm $< r <$ 110 cm. An impressive photo of the TEC can be seen in Fig. 39, where the petal structures can also be seen.

### 2.4.1. CMS strategy to withstand the LHC radiation environment

This section very briefly describes the radiation-hardness precautions of the CMS Tracking detector. The radiation environment at luminosities of $10^{34}$ cm$^{-2}$ s$^{-1}$ can be translated to integrated fluences[20] on the order of $\Phi_{eq} = 10^{13}$ n$_{1\ \mathrm{MeV}}$/cm$^2$ in the outer strip tracker and $\Phi_{eq} = 1 \times 10^{14}$ n$_{1\ \mathrm{MeV}}$/cm$^2$ in the inner strip tracker volume for the full operation period of 10 years. The pixel detectors are expected to be subjected to even $\Phi_{eq} = 3 \times 10^{14}$ n$_{1\ \mathrm{MeV}}$/cm$^2$ per year. These numbers are derived from simulations.

*Radiation tolerance pixel sensors*: The pixel detector's sensor and chip design is described in detail in Refs. [30,35]. The pixel sensors are processed in planar technology, n-in-n (n+ pixelated implants on n-bulk). The n-bulk is oxygenated to reduce acceptor creation during irradiation, thereby reducing the final depletion voltage. In this design, electrons are collected and the high field side will reside, after type inversion, on the pixel side, enabling an under-depleted operation with less signal.[21]

*Radiation tolerance silicon strip sensors*: All silicon strip sensors are single-sided with AC-coupled readout and p+ strips biased through polysilicon resistors, based on the planar process. Pitches range from 80 to 183 µm without any intermediate strips. The substrate is non-oxygenated floatzone n-type silicon made from 6 in. diameter wafers. Within the high-radiation environment of LHC, all sensors will undergo type inversion, as discussed in Section 1.3. The main strategies of CMS to ensure the radiation hardness of silicon strip sensors consist of

1. delaying the bulk type inversion and achieving $V_{FD}$ always below 400–500 V;
2. the use of stable sensors with respect to high voltage and
3. the reduction of surface damage.

The full depletion voltage vs. fluence, time and temperature is kept under control by:

- Freezing out all reverse annealing by operating all sensors at sub-zero temperatures.

[20] Reminder: fluence numbers are always given in 1 MeV neutron equivalent/cm$^2$ [$\Phi_{eq}$] = n$_{1\ \mathrm{MeV}}$/cm$^2$.

[21] In n-in-n under-depletion mode, the non-depleted zone stays on the backside only reducing the active volume but with the depletion zone at the segmented pixel face.

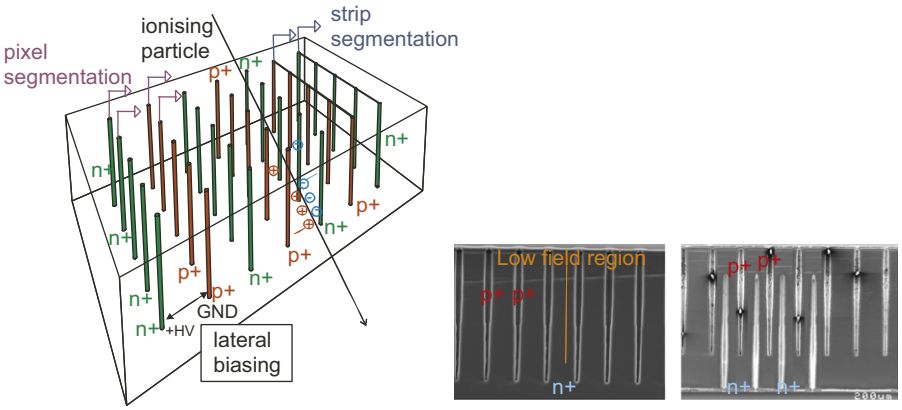


**Fig. 42.** Deviating from the standard planar sensor process, deep holes are etched into the silicon to achieve holes, finally serving as electrode junctions to span the depletion zone in a horizontal way instead of the standard vertical one. The electrons and holes travel a much shorter distance and are therefore less sensitive to trapping. The picture on the right shows a cut through 3D sensors. The 3D single column type (STC) (left) suffers from a low field region between columns due to lateral depletion. The 3D double-sided double type columns (DDTC) (right) are more complicated but have a full field over the whole volume. Courtesy of CNM-IMB (CSIC), Barcelona.

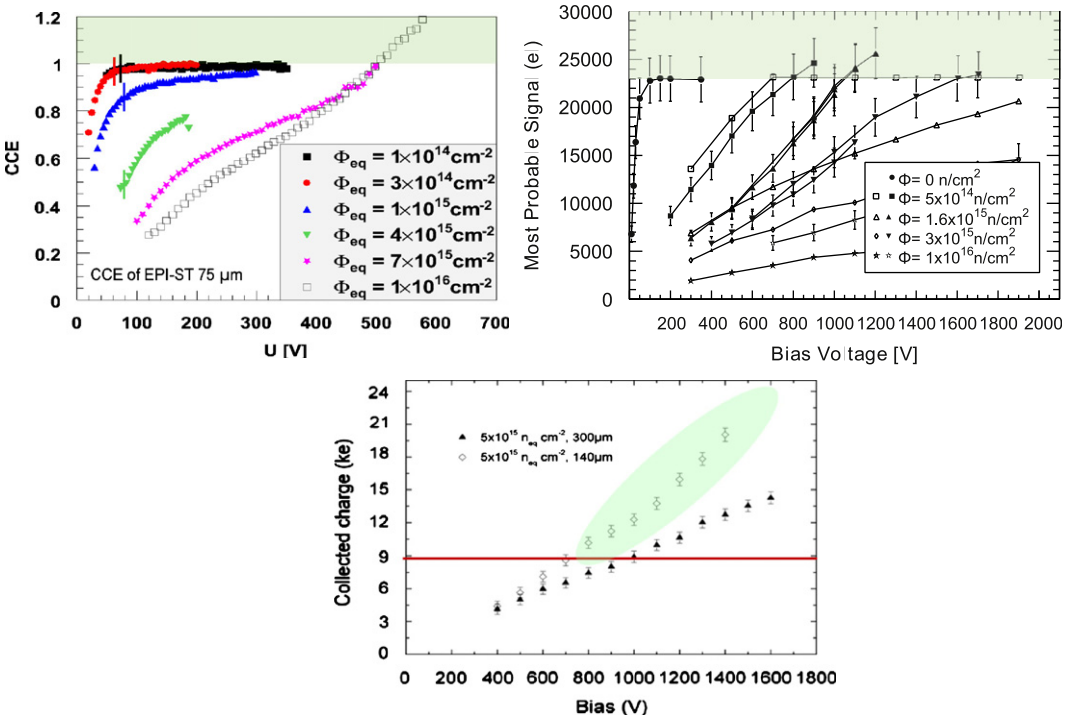


**Fig. 43.** Several groups claim to collect more charge after irradiation than before and even claim to collect more charge than a MIP can deposit in the given material volume. The first plot [42] shows a higher signal in n-EPI material after irradiation, the second [43] a higher signal in p-FZ sensors after neutron irradiation (reactor Ljubljana). The last [44] shows a higher signal in a p-FZ 140 µm thin sensor with respect to the 300 µm thick sensor and also with respect to the charge deposited by a MIP in the corresponding volume (after $5 \times 10^{15}$ $n_{1\ MeV}/cm^2$ with 25 MeV-p). Clear signatures of charge amplifications have been identified.

- Exploiting beneficial annealing with a controlled warm up during the maintenance periods.
- Starting with relatively low resistivity silicon to reach the inversion time late and ending with about the same depletion voltage as the initial one.

This goal is achieved by a dedicated "intelligent" thermal screen around the Tracker volume, which guarantees a cold running (active cooling) inside and stable temperature (PID controlled heating foils) outside.

The voltage robustness was largely the responsibility of the vendor by avoidance of any sharp corners; deep implants; a large active n++ edge and a metal overhang[22] over the strips; and a floating guard ring.

Surface degradation was minimized by the use of ⟨1 0 0⟩ oriented silicon wafers with fewer dangling bonds than standard ⟨1 1 1⟩ silicon.

An exhaustive description can be found in Ref. [38].

[22] High fields at the p+ implants were shifted towards the metal strips into the $SiO_2$ insulation where the breakdown voltage is 20 times higher ($V_{break}(Si) = 30\ V/\mu m$ $V_{break}(SiO_2) = 600\ V/\mu m$).

*Radiation tolerant electronics*: The radiation tolerance of the custom-made electronic ASICS was given by deploying dedicated design strategies[23] within the newly developed 0.25 μm feature size chip processing. The technology is also called "deep submicron" or "quarter micron[24]" and is much more radiation tolerant than any former chip generation. The detailed effect and technology exploitation (design strategies) is described in Refs. [36,37].

## 3. Outlook and examples of recent R&D

For future applications, with even higher radiation, the currently deployed detectors are not sufficiently radiation hard. New materials and detector schemes had to be developed mainly within the RD50 and LHC collaboration efforts. Fig. 40 gives a good overview of the current understanding of the signal achievable in different silicon sensors and materials. Recent overviews are in Refs. [39,40].

Clearly, at SLHC fluences around $10^{16}$ 1 MeV$_{eq}$/cm$^2$, current LHC silicon sensor technologies are not mature enough to operate, and new solutions are under research and development.

It becomes clear that the current p-in-n FZ material in primary use (for strip sensors) is probably no longer adequate, and future strip sensors may use n-in-n or n-in-p sensors. It seems that trapping is less pronounced for electron readout than for hole readout [8,41]. As previously mentioned, Fig. 41 teaches us that at very high fluences, trapping becomes the dominant damage factor (reducing signal), and different particle radiations result in the same effective CCE.

*3D sensors*: An escape route is given with 3D silicon sensors, where column-like electrodes penetrate the substrate instead of strips at the surface, therefore decreasing electrode spacing while utilizing the full volume [45]. The path minimizing the trapping probability allows for substantial signal with fast signals after fluences of $10^{15}-10^{16}$ n$_{1\ \mathrm{MeV}}$/cm$^2$. Due to the resulting lateral depletion, the concept also allows for low operation voltages. The main drawback is the resulting high channel capacitances. A scheme and an actual photo of two different 3D sensor configurations can be seen in Fig. 42.

*Charge amplification in silicon sensors*: In the last two years, different groups have reported higher CCE after irradiation than before, which is completely incompatible with any trapping model. In several cases, more charge per volume has been recorded than a MIP deposits due to ionization. Fig. 43 shows three examples hinting at a charge *amplification* mechanism. It is now of utmost importance to evaluate if the charge amplification is really the desired modus operandi for silicon sensors in the HEP environment. How are the leakage current and the noise affected, and what is the resulting effective signal to noise? Further dedicated studies are needed.

## References


[1] C. Kittel, Introduction to Solid State Physics, Fourth Edition, John Wiley & Sons, Inc., New York, London, Sydney, Toronto.
[2] S.M. Sze, Physics of Semiconductor Devices, John Wiley and Sons, 1985.
[3] A. Peisert, Silicon microstrip detector, Instrumentation in High-Energy Physics, World Scientific, 1992.
[4] G. Lutz, Semiconductor Radiation Detectors, Springer, 1999.
[5] F. Hartmann, Evolution of Silicon Sensor Technology in Particle Physics; Series: Springer Tracts in Modern Physics; 〈http://www.springer.com/series/426〉, vol. 231, 2009, ISBN: 978-3-540-25094-4.
[6] J. Marczewski, in: C.A. Ambroziak (Ed.), Bulk Silicon Detectors of Ionizing Radiation. The Role of the Depletion Layer, Institute of Electron Technology, Warsaw, 2005 ISBN 83-914179-5-6.
[7] The Particle Data Group 〈http://pdg.lbl.gov/〉.
[8] 〈http://www.cern.ch/rd50〉.
[9] M. Moll, Radiation Damage in Silicon Particle Detectors, DESY-THESIS-1999-040, Universität Hamburg, 1999.
[10] R. Wunstorf, Ph.D. Thesis, DESY-FH1K-92-01, 1992.
[11] R. Wunstorf, IEEE Transactions on Nuclear Science NS-44 (3) (1997).
[12] A. Dierlamm, Irradiation qualification of CMS tracker components, in: 4th International Conference on Radiation Effects on Semiconductor Materials, Detectors and Devices, Florence 2002, Nuclear Instruments and Methods in Physics Research Section A 514 (2003).
[13] A. Dierlamm, Ph.D. Thesis, IEKP-KA/2003-23, Untersuchungen zur Strahlenhärte von Siliziumsensoren, 2003.
[14] I. Pintilie, et al., Nuclear Instruments and Methods in Physics Research Section A 611 (1) (2009) 52.
[15] A. Affolder, P. Allport, G. Casse, Nuclear Instruments and Methods in Physics Research Section A 604 (1–2) (2009) 250.
[16] A.S. Schwarz, Physics Report 238 (1&2) (1994) 1.
[17] E. Belau, et al., Nuclear Instruments and Methods in Physics Research Section A 217 (1983) 23.
[18] The earliest successful use of SMDs in high energy physics experiments was by the NA11 collaboration at CERN, which did so much to develop these devices. J. Kemmer, Nuclear Instruments and Methods in Physics Research 169, 499 (1980). B. Hyams, et al., Nuclear Instruments and Methods in Physics Research 205, 99 (1983).
[19] The DELPHI Silicon Tracker Group, Nuclear Instruments and Methods in Physics Research Section A 412 (1998) 304.
[20] M. Krammer, T. Bergauer, private communication.
[21] F. Bedeschi, et al., A Silicon Vertex Detector for CDF, CDF Note 362, 1985.
[22] A. Sill, et al., Nuclear Instruments and Methods in Physics Research Section A 447 (2000) 1.
[23] J. Incandela, private communication.
[24] Layer 00 was first proposed by J. Incandela, N. Bacchetta, R. Snider, D. Stuart. It is described in C.S. Hill, CDF Collaboration, Nuclear Instruments and Methods in Physics Research Section A 530 (2004) 1; T.K. Nelson, CDF Collaboration, International Journal of Modern Physics A 16S1C (2001) 1091.
[25] The ISL was first proposed by D. Stuart, J. Incandela, A. Yagil. It is described in A. Affolder, et al., Nuclear Instruments and Methods in Physics Research Section A 453 (2000) 84.
[26] F. Hartmann, et al., The Intermediate Silicon Layers Detector at CDFII Design and Progress–Proceedings of VERTEX '98, Nuclear Instruments and Methods in Physics Research Section A 435(1+2) (1999).
[27] F. Hartmann, Ph.D. Thesis, IEKP−KA/00−11, Entwicklungsarbeit am Spurendetektor für das CDF Experiment am Tevatron, 2000.
[28] CDF II Collaboration, Technical Design Report, FERMILAB−Pub−96/390−E, 1996.
[29] E. Meschi, et al., Nuclear Instruments and Methods in Physics Research Section A 409 (1998) 658.
[30] R. Adolphi et al., By CMS Collaboration, The CMS experiment at the CERN LHC, JINST 0803:S08004, 361 pp; The CMS Collaboration, The CMS experiment at the CERN LHC, JINST 3:S08004, 2008, 361 pp.
[31] CMS Collaboration, Technical Proposal, CERN/LHCC 94−38, 1994; CMS Collaboration, Addendum to the CMS Tracker, CERN/LHCC 200−016, 2000.
[32] D. Abbaneo, et al., Nuclear Instruments and Methods in Physics Research Section A 518 (2004) 331.
[33] F. Hartmann, on behalf of the CMS Silicon Tracker Collaboration, The Construction of the CMS Tracker, Nuclear Instruments and Methods in Physics Research Section A 572 (1) (2007) 73.
[34] G. Sguazzonia, on behalf of the CMS Silicon Tracker Collaboration, Nuclear Physics B (Proceedings Supplements) 177–178 (2008) 328.
[35] A. Dominguez, et al., Nuclear Instruments and Methods in Physics Research Section A 581 (2007) 343.
[36] P. Jarron, et al., Nuclear Physics B (Proceedings Supplements) 78 (1999) 625.
[37] L.L. Jones, et al., The APV25 deep submicron readout chip for CMS detectors. 1999, Prepared for 5th Workshop on Electronics for the LHC Experiments (LEB 99), Snowmass, CO, 20–24 September 1999.
[38] N. Demaria, et al., Nuclear Instruments and Methods in Physics Research Section A 447 (2000) 142;
R. Dell'Orso, Recent results for the CMS Tracker Silicon Detectors, in: Proceedings of the 2000 Nuclear Science Symposium and Medical Imaging Conference, 2000;
L. Bellucci, Nuclear Instruments and Methods in Physics Research Section A 462 (2001) 243;
L. Borrello, A. Messineo, E. Focardi, A. Macchiolo, Sensor design for the CMS Silicon Strip Tracker, CMS NOTE 2003/020, 2003.
[39] M. Moll, Recent advances in the development of radiation tolerant silicon detectors for the Super−LHC, Presented at 11th ICAPTT Conference, Como, 5–9 October 2009.
[40] F. Hartmann, Semiconductor sensors, in: Proceedings of the Vienna Conference of Instrumentation VCI 2010; F. Hartmann, Nuclear Instruments and Methods in Physics Research Section A: Accelerators, Spectrometers, Detectors and Associated Equipment 628 (1) (2011) 40.
[41] G. Casse, A. Affolder, P.P. Allport, H. Brown, I. McLeod, M. Wormald, Nuclear Instruments and Methods in Physics Research Section A 636 (1) (2011) S56.


[23] Developed at CERN.

[24] At a feature size of 0.25 μm and below, chips start to be sufficiently radiation tolerant for LHC operation.

[42] J. Lange, J. Becker, D. Eckstein, E. Fretwurst, R. Klanner, G. Lindström, Charge collection studies of proton_irradiated n- and p-type epitaxial silicon detectors, in: Proceedings of the 11th ESSD, 2009, vol. 624 (2), 2010 pp. 405–409.
[43] I. Mandić, et al., Nuclear Instruments and Methods in Physics Research Section A 612 (2010) 474.
[44] G. Casse, A. Affolder, P.P. Allport, H. Brown, M. Wormald, Enhanced efficiency of segmented silicon detectors of different thicknesses after proton irradiations up to $1 \times 10^{16} n_{eq}$ cm$^2$, Nuclear Instruments and Methods in Physics Research Section A 624 (2) (2010) 401.
[45] Introduced by S.I. Parker et al., Nuclear Instruments and Methods A 395 (1997) 328.